8-2010

Simultaneous Seismic Imaging and Inversion Using an Inverse Scattering Algorithm for One Dimensional Media

Ashley Ciesla

Abstract

The goal of this thesis is to test the capability and efficiency of an inverse scattering algorithm for imaging seismic data. The algorithm we are investigating simultaneously images and inverts one-dimensional, one-parameter (velocity), acoustic reflection data. The algorithm does not require a velocity model or any other *a priori* information about the medium under investigation, the only input being a reference velocity (the speed of sound in water) and the data collected in the experiment. We assume that the data contains no source wavelet and all other events except primary reflections have been removed in preprocessing. We simulate two types of data: full frequency spectrum impulse data, using the Dirac delta function, and band-limited data, using the Sinc function. The data is collected over four different models that exemplify different conditions that can be found in a one-dimensional medium with variable velocity. We show that the algorithm can precisely locate the interfaces and discover the correct velocity changes at those interfaces. We also compare this algorithm with the inverse scattering leading order imaging algorithm that Shaw presented in *An inverse scattering series algorithm for depth imaging of reflection data* (See [12]). The latter uses certain imaging terms from the inverse scattering series to approximate the location of the interfaces in the unknown medium without providing any information about the change in the velocity at those interfaces. We show that the present algorithm located the interfaces more accurately in all the test cases.

MONTCLAIR STATE UNIVERSITY

SIMULTANEOUS SEISMIC IMAGING AND INVERSION USING AN INVERSE SCATTERING ALGORITHM FOR ONE DIMENSIONAL MEDIA

by

ASHLEY CIESLA

A Master's Thesis Submitted to the Faculty of

Montclair State University

in Partial Fulfillment of the Requirements for the Degree of

Master of Science

with a Concentration in Pure and Applied Mathematics

August 2010

College of Science and Mathematics
Department of Mathematical Sciences

Thesis Committee:

[redacted]

Bogdan Nita
Thesis Sponsor

[redacted]

Robert Prezant
Dean of College of Science and Mathematics

8/26/10

Date

[redacted]

Arup Mukherjee
Committee Member

[redacted]

Philip Yecko
Committee Member

[redacted]

Helen M. Roberts
Department Chair

Contents

List of Figures

1 Introduction

As natural resources are rapidly depleting, the search for more sophisticated methods of discovery, that also improve efficiency, causes a dilemma. This is especially true when improving methods exploration that handle searching beyond what is visible not only to the naked eye, but to cameras as well, no matter how small. There are many instances where x-ray vision would be a convenient way of looking through surfaces to search for whatever it is we are looking for - and there are a lot of different disciplines that could benefit. Obviously, however, this is impossible and we must find ways of approximating what is underneath different surfaces using the tools that are available to us. We know that sound will penetrate not only a surface but its sub-surfaces. If we record the sound waves that interact with these sub-surfaces, we can analyze them and discover the location and the properties of hidden targets.

Although we will be mainly discussing earth models in this paper, the utility of these methods reaches beyond sub-surface imaging. Consider medical ultrasound imaging, the same type of methods are being used with slight variations. Therefore, it is possible to adapt the algorithm studied in this thesis to medical (and other) applications.

Seismic exploration is useful for characterizing sub-surface geology. This is accomplished by creating a source and receiver experiment. In this experiment, there is a man-made wave, usually produced by an explosion, that is recorded after it interacts with the different layers of a medium. These recordings contain information about the internal structure of the earth. For example, the time of arrival contains information about the depth of the interfaces – the later the signal returns, the deeper the target– and the amplitude of the returning wave contains information about the parameter changes (velocity, density, etc.) at the interfaces. The collected data is analyzed to extract as much useful information as possible.

Modern algorithms rely on simple formulas to determine such information. For example, the depth of an interface is determined using a relation similar to the classical distance

formula : $distance = \frac{arrivaltime}{2} \times velocity$. In consequence, these algorithms require the velocity of propagation of the acoustic wave through all the earth structures in order to determine their position. Such velocity is *a priori* unknown and it is usually approximated or guessed, sometimes very poorly. The results, when such errors occur, are false images which lead to mislocated targets. Errors due to the use of an inappropriate velocity model can be reduced or even eliminated if the methods for processing data do not rely on estimates or assumptions about the structure or properties of the medium under investigation. This will lead to more accurate approximations and will avoid the previously noted effects of error.

Currently, the only tool that has the ability to supersede the requirement for a velocity model in seismic imaging is using inverse scattering theory. The method, derived from inverse scattering theory, reconstructs the scattering potential as a series which, when convergent, will output a complete map (structure and properties) of the medium properties from the full data set only (See [16]). However, there is no current method for analyzing its convergence and simple numerical analysis [2] has indicated that the full series might be divergent for high contrast earth layers.

To combat the convergence issue as well as the computational difficulties arising from using a full data set for seismic processing, a method of isolating convergent subseries was presented (See [16] and references therein). The goal of this approach was to find subseries which would perform only a specific part of the full inversion, part which would correspond to a regular seismic processing task. The subseries could have better convergence properties than the full series and, since only a piece of the data would be processed, the method would be faster and computationally less expensive. The four initial tasks are 1. free surface elimination 2. internal multiple elimination 3. imaging and 4. inversion or amplitude determination. What is important is that the subseries performing these tasks would preserve the need for data and information about the reference medium only and would avoid requiring *a priori* knowledge about the medium under investigation.

For the first two tasks, free surface and internal multiple elimination, model type independent algorithms have been found and applied extensively in the oil industry (See e.g. [14] and [16] and references therein). For the third task of imaging the reflectors at depth, algorithms have been found and tested for one and multi-dimensional acoustic media (See e.g. [5], [6], [7], [11], [12], [16]). For the fourth task of correcting the amplitude of the events in the data (inversion) several results have been obtained for one and multi-dimensional acoustic or elastic media [17]. In 2009, Nita [10] found a subseries which captures both imaging and inversion terms to perform the third and fourth tasks simultaneously. More importantly, besides the leading order imaging terms that where the basis for the imaging subseries presented before in [12], this subseries includes lower order imaging terms and hence has the potential of offering better results when imaging high contrast interfaces.

In this thesis, we show the results from running numerical tests on the simultaneous imaging and inversion algorithm presented in [10]. Among the tests we perform, we use different types of data (full frequency spectrum and band-limited) and various models to capture the characteristics of several earth configurations (different number of layers, different velocity contrasts and velocity inversions).

The inverse scattering algorithms for seismic processing assume that the source signature has been deconvolved from the data, source and receiver ghosts (free surface effects due to the up-going wave from the source and the down-going wave to the receiver, respectively) have been eliminated and that each previous task has been completed before a new one is started. For example, the imaging algorithm assumes that free surface and internal multiple reflections have also been removed (in addition to source signature and ghosts) and so, at this step, the data only consists of single reflections. This is the usual path of data processing in seismic exploration.

2 Objectives

Our first goal was to create a program for simulating a one-dimensional wave propagation in an acoustic one-parameter medium with any number of interfaces. This program only takes in consideration primary (single) reflections and ignores any other event (like free surface interactions or multiple reflections). Next, we chose various earth models which exhibit different number of interfaces and velocity contrasts across those interfaces, including velocity inversions. We then used the program to simulate data acquisition in a seismic experiment over these earth models. We used two different waveforms for the experiments, first, the Dirac delta function to simulate a full frequency spectrum impulse response, and then the Sinc function to simulate a more realistic band-limited signal.

Then, we input the simulated data into the algorithm for simultaneous imaging and inversion. Because of the multitude of models and waveforms used to produce the data, we expect these tests to give us a good characterization of the capabilities and the efficiency of the algorithm. Finally, we compared our results with the results obtained by running the same data set through the leading order imaging subseries algorithm described in [12]. We show that our algorithm is able to perform better in some cases of extreme velocity contrasts and offer an explanation for this behavior.

3 Background

3.1 Theoretical Development of Inverse Scattering Series

Inverse scattering theory is a framework for determining the characteristics of an object from measurement data of waves or particles scattered from that object. In seismic exploration, inverse scattering has been used successfully to process data with the prospect of finding the structure and characteristics of the medium in question. Scattering theory was derived from perturbation methods and is a form of perturbation analysis [13]. The theoretical development [16] starts off with the differential equations describing acoustic or elastic wave propagation in an actual and a reference medium,

$$\mathbf{LG} = -\mathbf{I} \tag{1}$$

and

$$\mathbf{L}_0\mathbf{G}_0 = -\mathbf{I}, \tag{2}$$

where $\mathbf{L}$, $\mathbf{L}_0$ and $\mathbf{G}$, $\mathbf{G}_0$ are the differential and Green's operators, respectively, and $\mathbf{I}$ is the identity operator. The perturbation operator, $\mathbf{V}$, and the scattered field operator, ψ_s, are defined as

$$\mathbf{V} = \mathbf{L} - \mathbf{L}_0, \tag{3}$$

$$\psi_s = \mathbf{G} - \mathbf{G}_0. \tag{4}$$

The above quantities, ψ_s, $\mathbf{G}_0$, $\mathbf{V}$, and $\mathbf{G}$, are related through the fundamental equation of scattering theory, the Lippmann–Schwinger equation [13]

$$\psi_s = \mathbf{G} - \mathbf{G}_0 = \mathbf{G}_0\mathbf{V}\mathbf{G}. \tag{5}$$

Relation (5) is valid everywhere, inside or outside the support of $\mathbf{V}$. The inverse problem in this case consists in determining $\mathbf{V}$ (both structural information (imaging) and amplitude information (inversion)) from measurements of ψ_s. Expanding Equation (5), by substituting $\mathbf{G} = \mathbf{G}_0 - \mathbf{G}_0\mathbf{V}\mathbf{G}$ into the right-hand side repeatedly, we obtain

$$\begin{aligned} \psi_s &= \mathbf{G}_0\mathbf{V}\mathbf{G}_0 + \mathbf{G}_0\mathbf{V}\mathbf{G}_0\mathbf{V}\mathbf{G} \\ \psi_s &= \mathbf{G}_0\mathbf{V}\mathbf{G}_0 + \mathbf{G}_0\mathbf{V}\mathbf{G}_0\mathbf{V}\mathbf{G}_0 + \mathbf{G}_0\mathbf{V}\mathbf{G}_0\mathbf{V}\mathbf{G}_0\mathbf{V}\mathbf{G} \\ &\vdots \end{aligned} \tag{6}$$

and so on. By repeating this process an infinite number of times, we imagine that we can drop the last term containing the Green's function of the actual medium, $\mathbf{G}$, in favor of an infinite series, and write the scattered field as

$$\psi_s \equiv \mathbf{G} - \mathbf{G}_0 = \mathbf{G}_0\mathbf{V}\mathbf{G}_0 + \mathbf{G}_0\mathbf{V}\mathbf{G}_0\mathbf{V}\mathbf{G}_0 + \cdots \quad . \tag{7}$$

This series, the forward scattering series, constructs the scattered field operator ψ_s, everywhere inside or outside the medium, as a sum of terms representing wave propagation in the reference medium, $\mathbf{G}_0$, and interactions with the inhomogeneity represented by the perturbation operator $\mathbf{V}$.

Restricting Equation (7) to the measurement surface we can rewrite it as

$$\mathbf{D} = \mathbf{G}_0\mathbf{V}\mathbf{G}_0 + \mathbf{G}_0\mathbf{V}\mathbf{G}_0\mathbf{V}\mathbf{G}_0 + \cdots \quad . \tag{8}$$

where all the quantities on the right side of the equation are also restricted to the measurement surface. Next we consider the expansion of the perturbation $\mathbf{V}$ as a series in orders of the data $\mathbf{D}$ and write

$$\mathbf{V} = \mathbf{V_1} + \mathbf{V_2} + \mathbf{V_3} + \ldots \tag{9}$$

where $\mathbf{V}_i$ are terms of order i in the data $\mathbf{D}$. This series is called the inverse scattering series. Plugging (9) into Equation (8) we find

$$\begin{aligned}\mathbf{D} = &\mathbf{G_0V_1G_0} + \mathbf{G_0V_2G_0} + \mathbf{G_0V_3G_0}\ldots \\ &+ \mathbf{G_0V_1G_0V_1G_0} + \mathbf{G_0V_1G_0V_2G_0} + \mathbf{G_0V_2G_0V_1G_0} + \ldots \\ &+ \mathbf{G_0V_1G_0V_1G_0V_1G_0} + \ldots \\ &+ \ldots .\end{aligned} \tag{10}$$

Equating like orders in the data in the equation above we find

$$\mathbf{D} = \mathbf{G_0V_1G_0} \tag{11}$$

$$0 = \mathbf{G_0V_2G_0} + \mathbf{G_0V_1G_0V_1G_0} \tag{12}$$

$$0 = \mathbf{G_0V_3G_0} + \mathbf{G_0V_2G_0V_1G_0} + \mathbf{G_0V_1G_0V_2G_0} + \mathbf{G_0V_1G_0V_1G_0V_1G_0} \tag{13}$$

$$\vdots .$$

These equations provide a recursive algorithm for calculating $\mathbf{V}_i$, and hence $\mathbf{V}$ via the series in Equation (9). What is amazing is that solving these equations only require knowledge of the recorded data, $\mathbf{D}$, and information about a chosen reference medium, $\mathbf{G}_0$. This eliminates the need of any *a priori* knowledge about the medium under investigation, especially the need of a velocity model to perform imaging.

The series in Equation (9) is too complicated to study. For example, even in a simple one dimensional acoustic medium, it's convergence properties are still unknown. The subseries method (See [16]) was developed to overcome these complications: rather than trying to solve this inverse problem in a single step (as the full series is supposed to do), look for subseries in the full series which will perform smaller steps in the inversion. These subseries would have smaller tasks to achieve, and hence they would also be easier to study, have known convergence properties and have targeted usefulness, possibly in combination

with other seismic methods (a history of this method can be found in [16]). We will look at some of these subseries for a one-dimensional, one-parameter acoustic medium in the next section.

3.2 One-dimensional Acoustic Media

In a one-dimensional acoustic medium with variable propagation speed and a whole space reference medium with constant propagation speed c_0, the perturbation operator [16] is

$$\mathbf{V} = k_0^2 \alpha(z) \tag{14}$$

where $k_0 = \frac{\omega}{c_0}$ with ω being the temporal frequency, $\alpha(z) = 1 - \frac{c_0^2}{c^2(z)}$ with z being the single variable dimension of the problem and $c(z)$ the velocity function describing the changes in the actual medium. The reference medium Green's function in the frequency domain is given by

$$\mathbf{G_0}(z_1|z_2;\omega) = \frac{e^{ik_0|z_1-z_2|}}{2ik_0} \tag{15}$$

where z_1 and z_2 are the positions of any two scatterers, or possibly the source and receiver. In this framework, the inverse problem is to solve for α, and the inverse scattering series (9) becomes

$$\alpha(z) = \alpha_1(z) + \alpha_2(z) + \alpha_3(z) + \ldots \tag{16}$$

where $\mathbf{V_i} = k_0^2 \alpha_i(z)$ for any $i \geq 1$.

With these assumptions we can calculate the first term in the inverse scattering series (See [12]) from Equation (11) to be

$$\alpha_1(z) = 4 \int_{-\infty}^{z} \mathbf{D}(z')dz', \tag{17}$$

where $\mathbf{D}(z')$ represents the wave propagation data that has been imaged to depth z'. This first term in the inverse scattering series represents the result of imaging the data with the

wrong velocity, c_0, and, in a simplistic way, is a realization of today's state-of-the-art methods which rely on a velocity model. Of course, this α_1 is just the first order approximation to the full model α and is the starting point for all inverse scattering methods. We will use this α_1 to calculate several terms in the inverse scattering series and to construct the subseries we are studying.

The second and third terms in the inverse scatting series (See [12]) are obtained from Equations (12) and (13), respectively:

$$\alpha_2(z) = -\frac{1}{2}\left(\frac{d}{dz}\alpha_1(z)\int_{-\infty}^{z}\alpha_1(z')dz' + \alpha_1^2(z)\right), \tag{18}$$

$$\begin{aligned}\alpha_3(z) &= \frac{3}{16}\alpha_1^3(z) + \frac{3}{4}\alpha_1(z)\int_{-\infty}^{z}\alpha_1(z')dz'\left[\frac{d}{dz}\alpha_1(z)\right] \\ &+ \frac{1}{8}\left(\alpha_1(z)\int_{-\infty}^{z}\alpha_1(z')dz\right)^2\left[\frac{d^2}{dz^2}\alpha_1(z)\right] - \frac{1}{8}\int_{-\infty}^{z}\alpha_1^2(z')dz'\left[\frac{d}{dz}\alpha_1(z)\right] \\ &- \frac{1}{16}\int_{-\infty}^{z}\int_{-\infty}^{z}\left[\frac{d}{dz'}\alpha_1(z')\right]\left[\frac{d}{dz''}\alpha_1(z'')\right]\alpha_1(z''+z'-z)dz''dz'.\end{aligned} \tag{19}$$

Other terms in the series can be obtained in a similar fashion. However, starting with the fourth term, the calculations are long and complicated and the benefits of performing these calculations are minimal. In the next sections, we show how the generalized subseries are formed by choosing imaging and inversion terms from the full inverse scattering series. This will be done for both the leading order imaging subseries of [12] and the simultaneous imaging and inversion subseries of [10].

3.2.1 Leading Order Imaging subseries

The second term in the inverse scattering series, Equation (18), contains two terms. As detailed in [15] these two terms can be interpreted as "self-interaction", $\alpha_1^2(z)$, and "separated", $\frac{d}{dz}\alpha_1(z)\int_{-\infty}^{z}\alpha_1(z')dz'$, scattering events. It was further found that separated terms with a single upward scattering point contribute to a subseries that images reflectors to

their correct spatial location, and self-interaction terms form the subseries that corrects the amplitude of α_1 towards that of α. If we wanted a subseries that only performs imaging, we should try to include as many such separated terms as possible and leave out any self-interacting terms or separated terms with two or more upward scattering points. With these considerations, the piece of α_2 that was picked to be part of the leading order imaging subseries (See [12]) was

$$\alpha_2^{IS_{LO}}(z) = -\frac{1}{2}\left(\frac{d}{dz}\alpha_1(z)\int_{-\infty}^{z}\alpha_1(z')dz'\right). \tag{20}$$

The third term in the inverse scattering series, Equation (19), contains several types of terms: self-interaction terms which correct the amplitude, separated terms which perform imaging and remove internal multiples, and mixed terms which perform coupled tasks. The piece of α_3 that was picked to be part of the leading order imaging subseries (See [12]) was

$$\alpha_3^{IS_{LO}}(z) = \frac{1}{8}\left[\frac{d^2}{dz^2}\alpha_1(z)\right]\left(\int_{-\infty}^{z}\alpha_1(z')dz\right)^2. \tag{21}$$

As before, this term represents only the leading order contributions corresponding to purely separated scattering events with a single upward scattering point. All subsequent terms in the inverse scattering series are broken down and selected in the same fashion. Summing all these leading order imaging pieces forms the leading order imaging subseries:

$$\alpha^{IS_{LO}}(z) = \alpha_1(z) - \frac{1}{2}\left[\frac{d}{dz}\alpha_1(z)\right]\left(\int_{-\infty}^{z}\alpha_1(z')dz'\right) + \frac{1}{8}\left[\frac{d^2}{dz^2}\alpha_1(z)\right]\left(\int_{-\infty}^{z}\alpha_1(z')dz\right)^2 + \ldots. \tag{22}$$

After analysis of the first three terms in the inverse scattering series, it was postulated that the generalized form of the subseries (See [12]) was

$$\alpha^{IS_{LO}}(z) = \frac{1}{2\pi}\int_{-\infty}^{\infty}\sum_{n=0}^{\infty}\frac{1}{n!}\left(-ik_0\frac{1}{2}\int_{-\infty}^{z}\alpha_1(z')dz'\right)^n\alpha_1(k_0)e^{ik_0z}dk_0. \tag{23}$$

The series in Equation (23) can be shown to converge for any values of it's parameters to the limit

$$\alpha^{IS_{LO}}(z) = \frac{1}{2\pi}\int_{-\infty}^{\infty} \alpha_1(k_0) e^{ik_0(z-\frac{1}{2}\int_0^z \alpha_1(z')dz')} dk_0. \tag{24}$$

The leading order imaging subseries terms act to correctly locate the interfaces that are mislocated in α_1 without altering the amplitude of α_1. However, starting with the third term, the inverse scattering series also contains higher order imaging terms consisting of separated scattering events that also have self-interaction components above the deepest scattering point. The conclusion is that the leading order imaging subseries offers only an approximation to α and a subseries which would take into consideration higher order imaging terms would give better results in specific cases. Some of these higher order terms are included in the subseries for simultaneous imaging and inversion of [10] which is presented in the next section.

3.2.2 Simultaneous Imaging and Inversion Algorithm

As with the leading order imaging subseries, the first term in the simultaneous imaging and inversion subseries is α_1 from Equation (17). For the second term in the subseries, the full α_2 in Equation (17) was used (See [10]) therefore including both imaging and inversion terms starting with this lowest possible order. Notice that this second term can be written in a simplified form as

$$\alpha_2(z) = -\frac{1}{2}\frac{d}{dz}\left[\alpha_1(z)\int_{-\infty}^{z} \alpha_1(z')dz'\right]. \tag{25}$$

This simplified form was the basis for the search for similar expressions in α_3 and beyond. For the third term in the subseries, the following piece of α_3 was selected

$$\alpha_3^{SII}(z) = \frac{1}{4}\alpha_1^3(z) + \frac{3}{4}\alpha_1(z)\int_{-\infty}^{z}\alpha_1(z')dz'\left[\frac{d}{dz}\alpha_1(z)\right] + \frac{1}{8}\left(\int_{-\infty}^{z}\alpha_1(z')dz\right)^2\left[\frac{d^2}{dz^2}\alpha_1(z)\right]. \tag{26}$$

This expression can also be simplified into

$$\alpha_3^{SII}(z) = \frac{1}{8}\frac{d^2}{dz^2}\left[\alpha_1(z)\left(\int_{-\infty}^{z}\alpha_1(z')dz'\right)^2\right] \tag{27}$$

therefore obtaining the same pattern as in α_2. Notice that this piece of α_3 contains not only the separated or imaging terms, as was the case for the leading order imaging subseries, but also self-interaction or amplitude correction terms. Moreover, instead of including leading order terms only, Nita included higher order imaging terms with the hypothesis that these terms will aid in imaging data with large, varying contrasts.

Putting together these terms and postulating that the same pattern will be available for selection from all inverse scattering series terms we arrive at the full expression of the subseries (See [10])

$$\alpha^{SII}(z) = \sum_{n=0}^{\infty}\frac{(-\frac{1}{2})^n}{n!}\frac{d^n}{dz^n}\left[\alpha_1(z)\left(\int_{-\infty}^{z}\alpha_1(z')dz'\right)^n\right]. \tag{28}$$

In [10] it is also shown that this series is convergent for all values of the perturbation operator and the limit is,

$$\alpha^{SII}(z) = \int_{-\infty}^{\infty}e^{ik_0 z}\int_{-\infty}^{\infty}\alpha_1(z')e^{-ik_0(z'+\frac{1}{2}\int_{-\infty}^{z'}\alpha_1(z'')dz'')}dz'dk_0. \tag{29}$$

This is the closed form of the subseries for imaging and inversion which will be used for the numerical tests.

4 Modeling Wave Propagation in 1D Acoustic Media

The differential equation that is used to describe acoustic wave propagation in a one dimensional acoustic homogeneous medium (See [8]) is

$$\frac{d^2u}{dz^2} - \frac{1}{c^2}\frac{d^2u}{dt^2} = 0 \tag{30}$$

where $u = u(z,t)$ and c is a constant. The equation does not include a source term and hence it only models the propagation of a given waveform and not how the waveform is created. The general solution of this equation (See [8]) is

$$u(z,t) = F(z-ct) + G(z+ct) \tag{31}$$

for arbitrary functions F and G. This expression represents the superposition of a left-travelling wave, $G(z+ct)$, and a right travelling wave, $F(z-ct)$.

By assuming that the variables in the solution u are separable we arrive at a simplified version of the wave equation (See [8])

$$\frac{d^2u}{dz^2} + \frac{\omega^2}{c^2}u = 0 \tag{32}$$

where ω is the temporal frequency.

This is the Helmholtz equation. It was shown in [8] that the solutions of this last equation take the form

$$u(z,\omega) = Ae^{ikz} + Be^{-ikz} \tag{33}$$

where, $A = A(\omega)$, $B = B(\omega)$ and $k = \frac{\omega}{c}$. In the time domain we can write

$$u(z,t) = \int_{-\infty}^{\infty} Ae^{ik(z-ct)} + Be^{-ik(z-ct)}d\omega \tag{34}$$

and notice that, consistent with the previous formula, $Ae^{ik(z-ct)}$ represents the right-travelling

wave and $Be^{-ik(z-ct)}$ represents the left-travelling wave.

4.1 Reflection and Transmission of Waves

When a wave propagating through a medium interacts with an interface, part of the wave will reflect back in the first layer and another part of the wave will transmit into the next layer. Once the transmitted part reaches the next interface, it will again split into a reflected part and a transmitted part. This process continues until the wave has completely dissipated. In a seismic experiment, the reflected parts are usually recorded and analyzed for information about the location of the interfaces and the changes in medium properties that occur at these interfaces. In this section, we show how to find formulas for the transmission and reflection coefficients representing the amplitudes of the transmitted and reflected waves, respectively.

At an interface, located say at $z = 0$, the total wavefield $u(z,t)$ is composed of three pieces: the incoming wave, the reflected wave and the transmitted wave. By definition, the incoming and the reflected waves are on the same side of the interface and the transmitted wave is on the opposite side. Therefore we can write

$$u(z,t) = \left\{ \begin{array}{ll} f_I(z-c_1t) + f_R(z+c_1t), & z<0 \\ f_T(z-c_2t), & z>0 \end{array} \right\} \tag{35}$$

where I, R, and T stand for the incoming, reflected and transmitted pieces respectively (See [8]). The continuity of displacement and momentum at the interface lead to two equations

$$\begin{aligned} f_I(c_1t) + f_R(c_1t) &= f_T(-c_2t) \\ f_I'(c_1t) + f_R'(c_1t) &= f_T'(-c_2t) \end{aligned}$$

which can be solved to find f_R and f_T

$$f_R(c_1 t) = \frac{c_2 - c_1}{c_2 + c_1} f_I(-c_1 t) \tag{36}$$

$$f_T(-c_2 t) = \frac{2c_2}{c_1 + c_2} f_I(-c_1 t) \tag{37}$$

The amplitudes of these waves are,

$$R = \frac{c_2 - c_1}{c_2 + c_1} \tag{38}$$

and

$$T = \frac{2c_2}{c_1 + c_2}. \tag{39}$$

are called the reflection and the transmission coefficients respectively.

In a regular seismic experiment there are many wave events that are recorded in the data set: direct arrival, primary (single reflections), free surface multiple reflections, source and receiver ghosts, internal multiple reflections. The current seismic exploration algorithms can only use the information in the primary reflections to determine the structure of the sub-surface. All other events are considered random or coherent noise and reduced or eliminated through a series of pre-processing steps. In this discussion, we are assuming that the data has been put through such pre-processing algorithms already and that the only parts of the wave that survived are the primary reflections. Therefore, when we create data for testing the imaging algorithms, we only create primary reflections.

4.2 Simulating Wave Propagation

In this section, we simulate data collected in a seismic experiment. We will use three models and two waveforms for our experiments, effectively creating six data sets that will be used in the simultaneous imaging and inversion algorithm. The waveforms that we are using represent a full frequency spectrum impulse described by the Dirac delta function

and a band-limited signal described by the Sinc function.

The Dirac delta function is a generalized function that has the value zero everywhere, except at $t = 0$, where its value is infinitely large in such a way that its total integral is equal to 1 (See [1], [3]). In the context of signal processing, it is often referred to as the unit impulse function (See Figure 1). We can therefore write

$$\delta(t) = \left\{ \begin{array}{ll} 0 & t \neq 0 \\ \infty & t = 0 \end{array} \right\}$$

such that

$$\int_{-\infty}^{\infty} \delta(t)\, dt = 1. \tag{40}$$

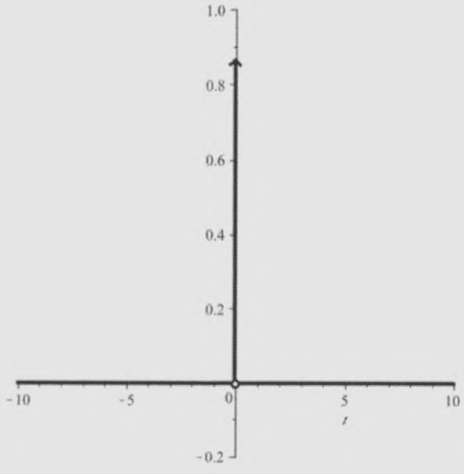

Figure 1: Dirac delta Function

Obviously there is no function that has these properties; the Dirac delta function can be rigorously defined either as a distribution or as a measure (See [1], [3]).

We can use the delta function to represent a full frequency spectrum impulse response in a seismic experiment. For example, for a simple medium (See Figure 2) which contains two layers (and therefore 2 interfaces), the data containing primary reflections only would have the form

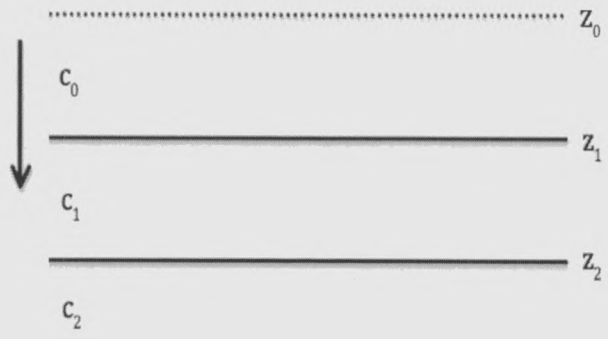

Figure 2: This earth model depicts two interfaces that are located at z_1 and z_2 with velocities of sound in the layers, c_0, c_1, and c_2. The source and receivers are assumed to be on the measurement surface $z_0 = 0$.

$$D(t) = R_1\delta(t-t_1) + R_2\delta(t-t_2) \tag{41}$$

where R_1 is the reflection coefficient of the first interface, t_1 is the arrival time of the first reflection, R_2 is the reflection coefficient of the second interface multiplied by the transmissions coefficients (forward and backward through the first interface) and t_2 is the arrival time of the second reflection. Notice that the rest of the events (multiple reflections inside of the middle layer) are not part of the data.

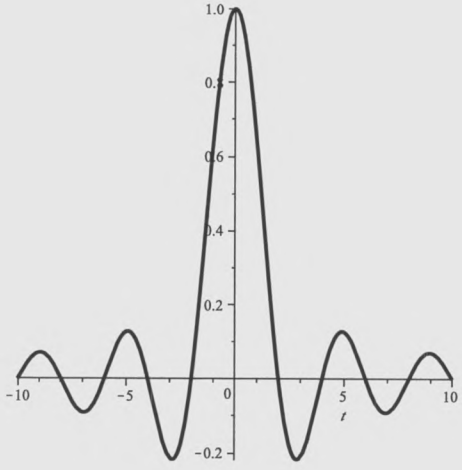

Figure 3: Sinc Function

The normalized Sinc function (See Figure 3) is defined as

$$Sinc(t) = \frac{\sin(\pi t)}{\pi t} \tag{42}$$

and has the same property as the Dirac delta function ([1], [3]), namely

$$\int_{-\infty}^{\infty} \frac{\sin(\pi t)}{\pi t}\, dt = 1. \tag{43}$$

The Sinc function represents a band-limited signal and it is closer to the actual representation of a waveform in seismic experiments - more than a Dirac delta function. For the model provided above, the data set would have the form

$$D(t) = R_1\, Sinc(t - t_1) + R_2\, Sinc(t - t_2) \tag{44}$$

where, as before, R_1 and R_2 are the reflection coefficients and t_1 and t_2 are the arrival times of the two reflections.

In order to test the accuracy of the approximations to the earth models we present, we first plot the the perturbation operator. Figure 5 shows the perturbation operator for our generalized earth model.

Notice, there are two "steps" in the plot of α. The location on the plot where each jump occurs is the corresponding location of the interface. In Figure 4, we see that there are 2 interfaces that occur at locations z_1 and z_2, respectively, which is where the plot of the perturbation operator also positions each interface. Also, the amplitude of the jumps depends on the velocity contrast between the reference velocity and the velocity in the following layer according to the formula for α,

$$\alpha(z) = 1 - \frac{c_0^2}{c^2(z)}$$

with z being the single variable dimension of the problem and $c(z)$ the velocity function

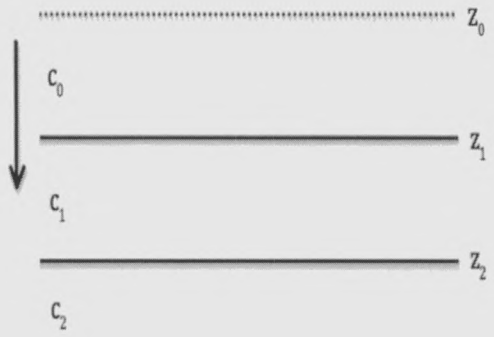

Figure 4: Earth Model

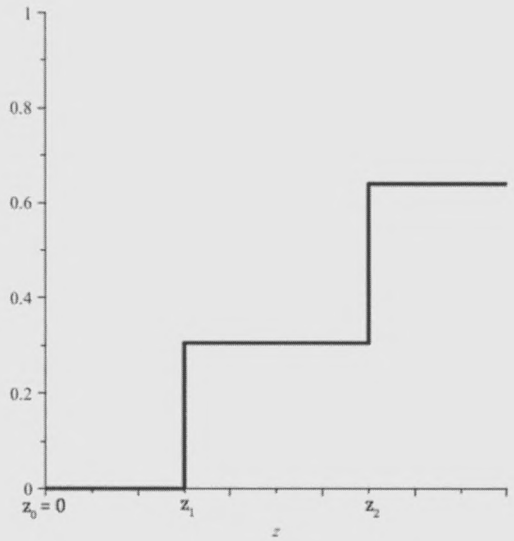

Figure 5: Perturbation Operator for Earth Model

describing the changes in the actual medium. In terms of amplitude size, the larger the change in velocity is between two layers, the larger the amplitude. Similarly, when there is a negative velocity inversion, the step will go down.

In the following sections we show the construction of the six data sets over three chosen earth models.

4.3 Model 1: Monotonic Increasing Velocity

The first model consists of three interfaces located in water at depths of $z_1 = 100$, $z_2 = 130$, and $z_3 = 160$ with the sound velocity inside of the layers having the values $c_0 = 1500$, $c_1 = 1650$, $c_2 = 1725$, and $c_3 = 1800$ (See Figure 6). The perturbation operator, α, for this earth model is shown in Figure 7.

The data in this case consists of three primary reflections. For a Dirac delta waveform the data has the formula,

$$D = \frac{1}{21}\delta(t-100) + \frac{88}{3969}\delta\left(t - \frac{1400}{11}\right) + \frac{178112}{8394435}\delta\left(t - \frac{38800}{253}\right) \qquad (45)$$

Figure 6: Earth Model 1

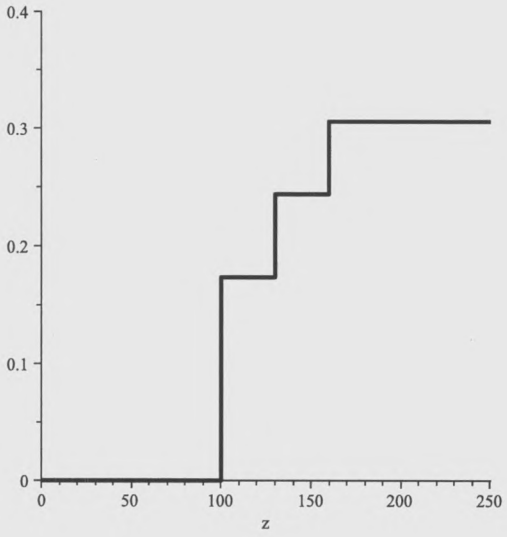

Figure 7: Perturbation Operator for Model 1

and, after transforming to depth domain, we obtain the picture in Figure 8.

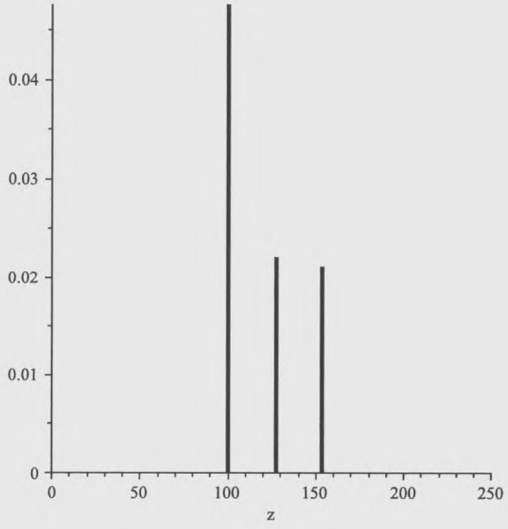

Figure 8: Model 1 Data obtained from a Dirac delta waveform

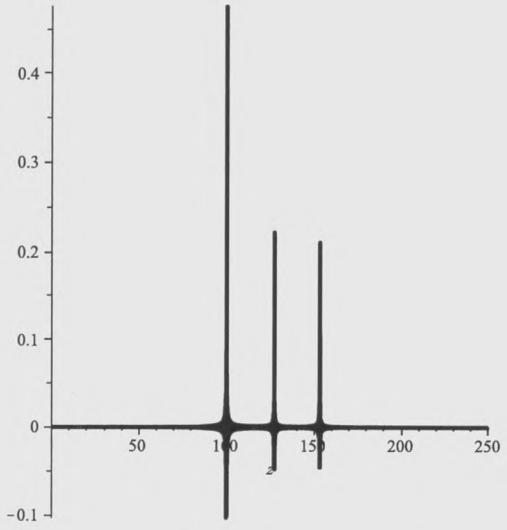

Figure 9: Model 1 Data obtained from a Sinc function waveform

For a Sinc function waveform the data has the formula,

$$D = \frac{1}{21} Sinc\,(t-100) + \frac{176}{3969} Sinc\left(t - \frac{1400}{11}\right) + \frac{356224}{8394435} Sinc\left(t - \frac{38800}{253}\right) \qquad (46)$$

Again, after transforming to depth domain, we obtain the plot in Figure 9.

Notice that, in both cases, the spikes are not placed at the correct depths, the transformation from time to depth domain being done with the reference velocity c_0 and not with the actual velocity of the earth model which is assumed to be unknown in all processing steps.

4.4 Model 2: Non-monotonic Velocity

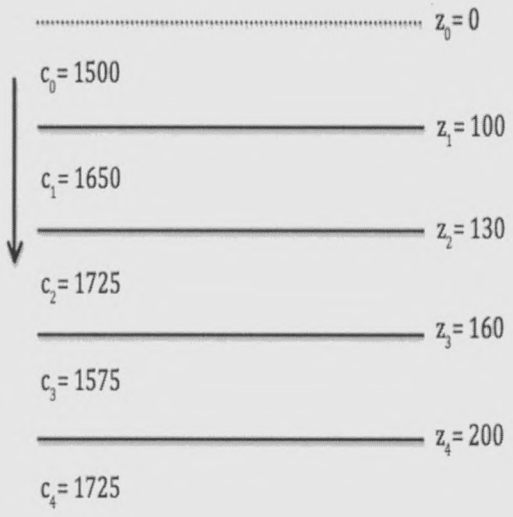

Figure 10: Earth Model 2

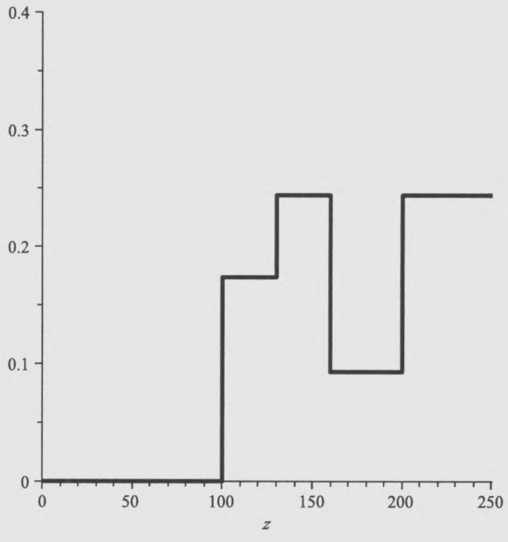

Figure 11: Perturbation Operator for Model 2

The second model consists of four interfaces located in water at depths of $z_1 = 100$, $z_2 = 130$, $z_3 = 160$ and $z_4 = 200$ with the sound velocity inside of the layers having the values $c_0 = 1500$, $c_1 = 1650$, $c_2 = 1725$, $c_3 = 1575$ and $c_4 = 1725$ (See Figure 10). This model is important to examine because, unlike the first example, the velocities in the layers are no longer monotonic. The perturbation operator for this earth model is shown in Figure 11.

The data in this case consists of four primary reflections. For a Dirac delta waveform

the data has the formula

$$\begin{aligned} D &= \frac{1}{21}\delta(t-100)+\frac{176}{3969}\delta\left(t-\frac{1400}{11}\right) \\ &- \frac{16192}{178605}\delta\left(t-\frac{38800}{253}\right)+\frac{8464}{93555}\delta\left(t-\frac{1017200}{5313}\right) \end{aligned} \tag{47}$$

and, as before, it can be plotted in the depth domain (See Figure 12). The negative am-

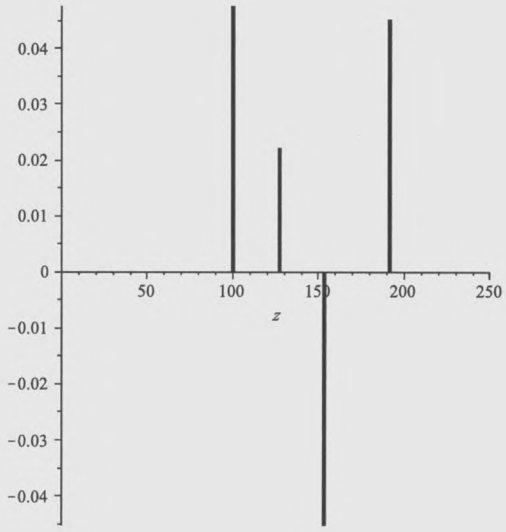

Figure 12: Model 2 Data obtained from a Dirac delta function waveform

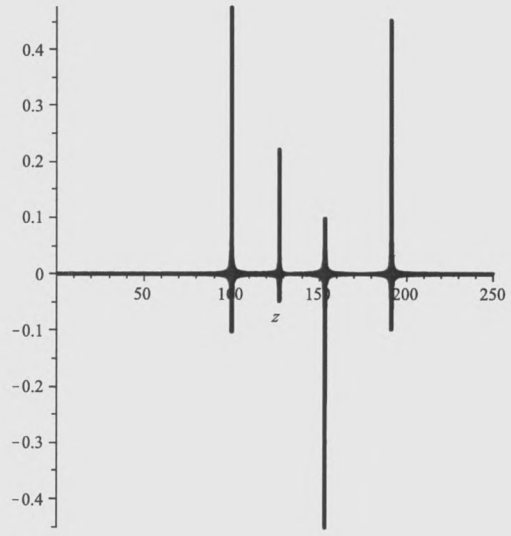

Figure 13: Model 2 Data obtained from a Sinc function waveform

plitude of the third pulse in Figure 12 is due to the velocity inversion occurring in our model: at the third interface, the velocity in the deeper layer is less then the velocity in the shallower layer.

For a Sinc function waveform the data has the formula

$$\begin{aligned} D &= \frac{1}{21}Sinc\,(t-100)+\frac{176}{3969}Sinc\left(t-\frac{1400}{11}\right) \\ &- \frac{16192}{178605}Sinc\left(t-\frac{38800}{253}\right)+\frac{8464}{93555}Sinc\left(t-\frac{1017200}{5313}\right) \end{aligned} \tag{48}$$

and, as before, can be plotted in the depth domain as in Figure 13.

Again, consistent with the picture above, the amplitude of the third pulse is negative

due to the velocity inversion from the model. The data in this case is not as "neat" as the Dirac delta data, but it represents a more "realistic" data set.

4.5 Model 3: Oscillating Velocity

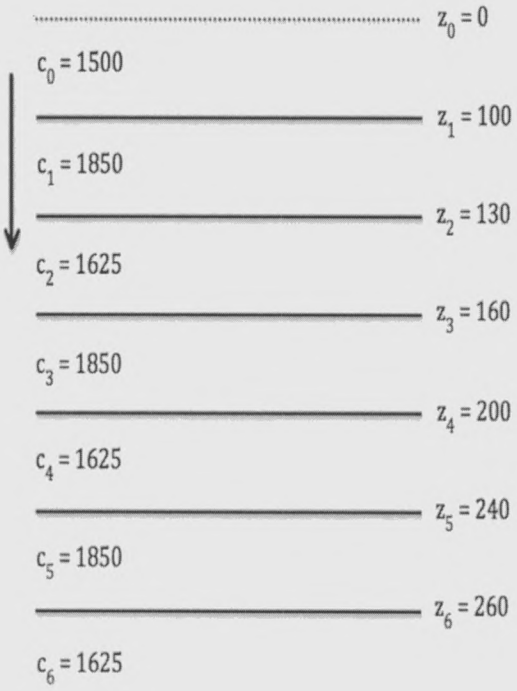

Figure 14: Earth Model 3

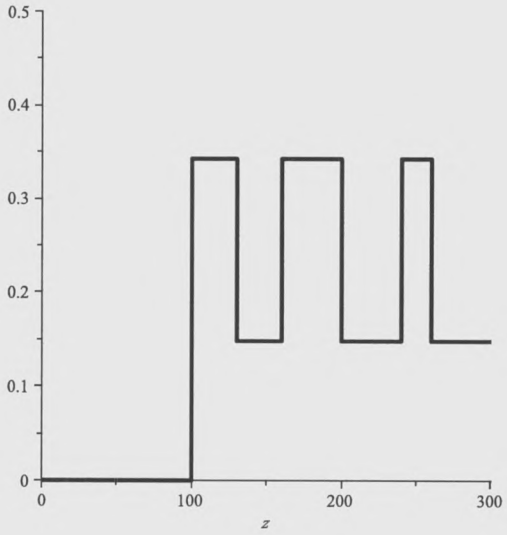

Figure 15: Perturbation Operator for Model 3

The third model consists of six interfaces located in water at depths of $z_1 = 100$, $z_2 = 130$, $z_3 = 160$, $z_4 = 200$, $z_5 = 240$, and $z_6 = 260$ with the sound velocity inside of the layers having the values $c_0 = 1500$ and then alternating between 1850 and 1625, respectively. This model is important to examine because it contains several velocity inversions and large velocity contrasts.The perturbation operator for this earth model is shown in Figure 15.

The data in this case consists of six primary reflections and, for a Dirac delta waveform,

it has the formula

$$\begin{aligned} D &= \frac{7}{67}\delta(t-100) - \frac{39960}{623971}\delta\left(t-\frac{4600}{37}\right) + \frac{768830400}{12055743691}\delta\left(t-\frac{73120}{481}\right) \\ &- \frac{14792296896000}{232929023853811}\delta\left(t-\frac{88720}{481}\right) + \frac{284603792279040000}{4500421669879482331}\delta\left(t-\frac{106480}{481}\right) \\ &- \frac{5745776963448729600000}{86952647083741478117251}\delta\left(t-\frac{114280}{481}\right). \end{aligned} \tag{49}$$

It is plotted in the depth domain in Figure 16. Notice that the pulses alternate between positive and negative amplitude, which is consistent with the alternating velocity inversions in the model.

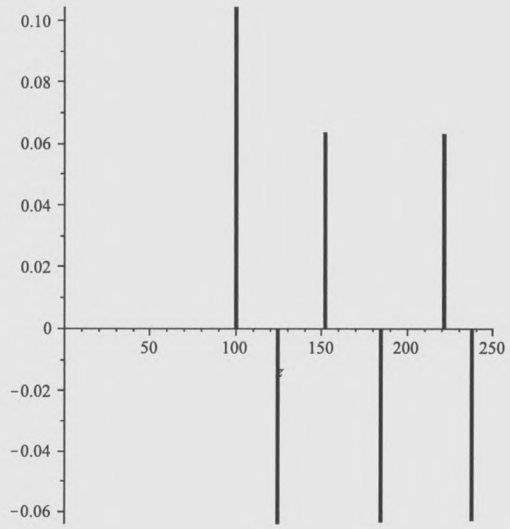

Figure 16: Model 3 Data obtained from a Dirac delta function waveform

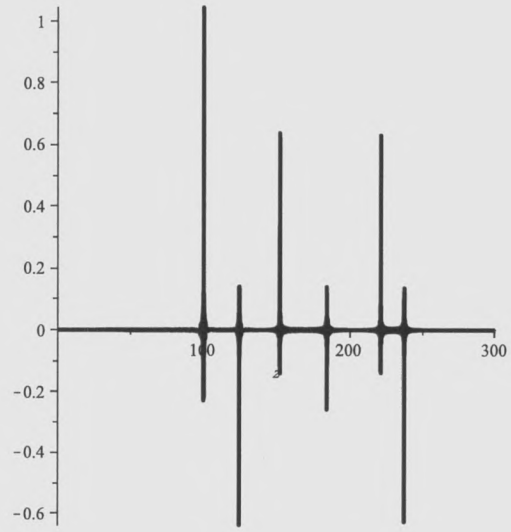

Figure 17: Model 3 Data obtained from a Sinc function waveform

For a Sinc function waveform the data has the formula

$$\begin{aligned} D &= \frac{7}{67}Sinc(t-100) - \frac{39960}{623971}Sinc\left(t-\frac{4600}{37}\right) + \frac{768830400}{12055743691}Sinc\left(t-\frac{73120}{481}\right) \\ &- \frac{14792296896000}{232929023853811}Sinc\left(t-\frac{88720}{481}\right) + \frac{284603792279040000}{4500421669879482331}Sinc\left(t-\frac{106480}{481}\right) \\ &- \frac{5745776963448729600000}{86952647083741478117251}Sinc\left(t-\frac{114280}{481}\right) \end{aligned} \tag{50}$$

After plotting it in the depth domain in Figure 17, we see again that the amplitudes of the pulses alternate between positive and negative values, which is consistent to the velocity inversions in earth model.

5 Numerical Tests of the Simultaneous Imaging and Inversion Algorithm

In this chapter we test the Simultaneous Imaging and Inversion algorithm using the six data sets described in the previous chapter. We will observe two main characteristics of the algorithm: its ability to correctly find the depths of the interfaces of the unknown medium and its ability to determine the correct amplitude of the perturbation operator.

The Simultaneous Imaging and Inversion Algorithm was shown in the previous section to have the formula (See Equation (29))

$$\alpha^{SII}(z) = \int_{-\infty}^{\infty} e^{ik_0 z} \int_{-\infty}^{\infty} \alpha_1(z') e^{-ik_0(z' + \frac{1}{2}\int_{-\infty}^{z'} \alpha_1(z'')dz'')} dz' dk_0, \tag{51}$$

where

$$\alpha_1(z) = 4 \int_{-\infty}^{z} \mathbf{D}(z')dz' \tag{52}$$

and where $\mathbf{D}(z')$ represents the data that has been imaged to depth z'.

5.1 Model 1: Monotonic Increasing Velocity

The first model, described in section 4.3, is shown in Figure 18 and the perturbation operator, α, is shown in Figure 19. The delta function data (See Equation (45)) is

$$D = \frac{1}{21}\delta(t-100) + \frac{88}{3969}\delta\left(t - \frac{1400}{11}\right) + \frac{178112}{8394435}\delta\left(t - \frac{38800}{253}\right).$$

Plugging this into Equation (52) for α_1, we obtain the first approximation to the perturbation operator α depicted in Figure 20. As expected, this first step is only able to find the first interface successfully. This will be true for all the others data sets because the actual medium coincides with the reference medium up to the first interface. However, since the reference medium is different then the actual medium for all the other layers, the locations

Figure 18: Earth Model 1

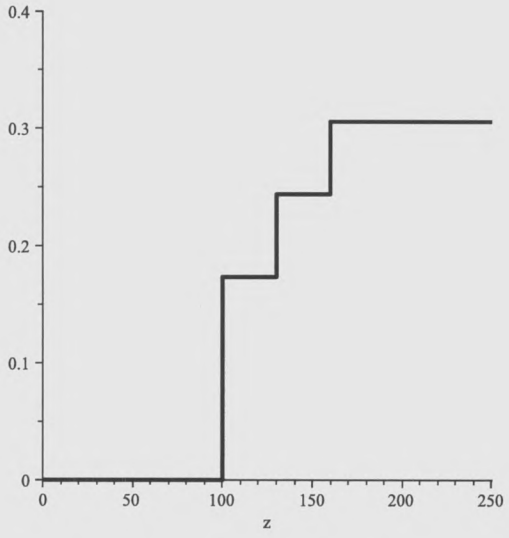

Figure 19: Perturbation Operator for Model 1

of the subsequent interfaces and the size of the perturbation from one layer to another will be miscalculated.

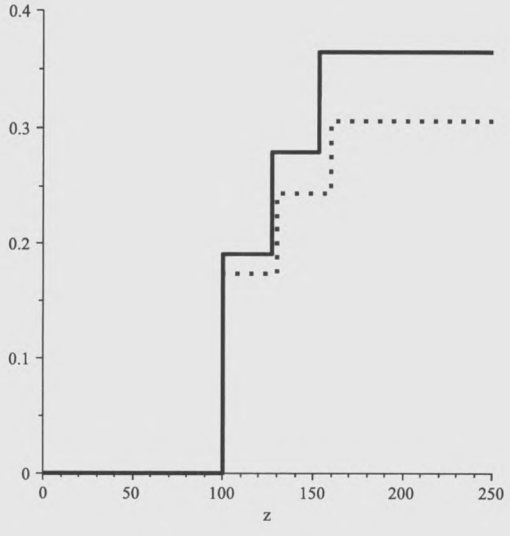

Figure 20: Plot of α_1 (solid) compared with α (dotted) for Model 1 and Dirac delta waveform input Data

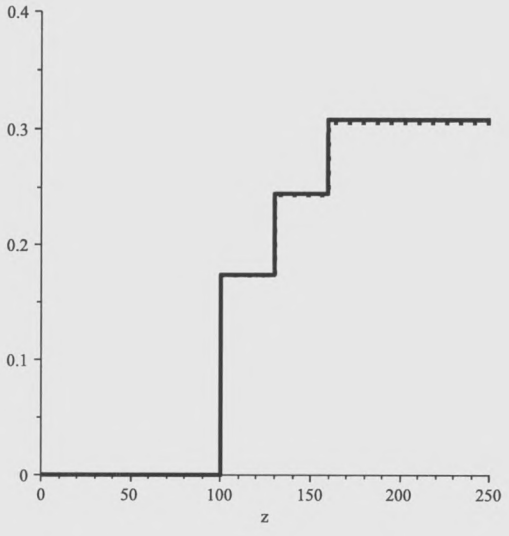

Figure 21: Plot of α^{SII} (solid) compared with α (dotted) for Model 1 and Dirac delta waveform input Data

Plugging the α_1 obtained in the first step into the algorithm in Equation (51) we obtain the approximation to the perturbation operator α depicted in Figure 21. We can see that the locations of all interfaces and the size of the perturbation from one layer to another have

been corrected and that the perturbation operator α is very well approximated.

The band-limited wave propagation data for Model 1 (See Equation (46)) is

$$D = \frac{1}{21}Sinc(t-100) + \frac{176}{3969}Sinc\left(t-\frac{1400}{11}\right) + \frac{356224}{8394435}Sinc\left(t-\frac{38800}{253}\right).$$

Plugging this into Equation (52) for α_1 we obtain the first approximation to the perturbation operator, α, depicted in Figure 22. As before, the first interface is accurately located but the location of the subsequent interfaces and the size of the perturbation from one layer to another is poorly approximated. We also notice the presence of the Gibbs phenomenon due to the use of the Sinc function to model the data.

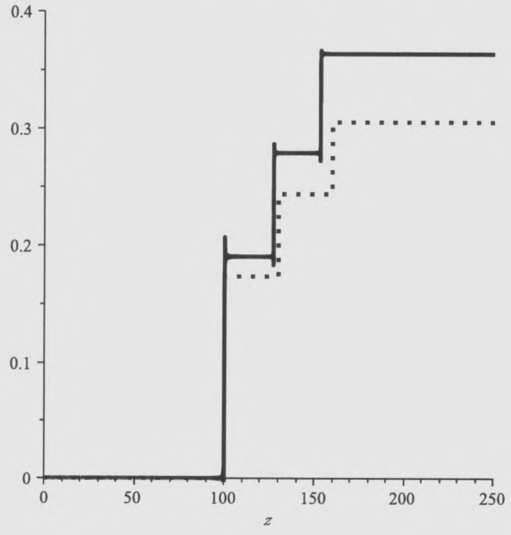

Figure 22: Plot of α_1 (solid) compared with α (dotted) for Model 1 and Sinc waveform input Data

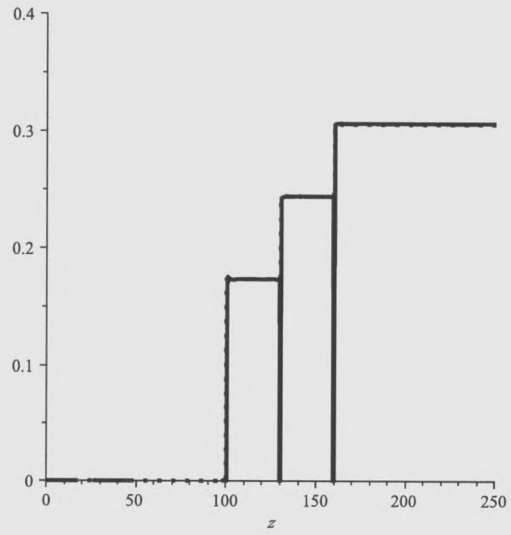

Figure 23: Plot of α^{SII} (solid) compared with α (dotted) for Model 1 and Sinc waveform input Data

Plugging the α_1, obtained in the first step, into the algorithm in Equation (51) we obtain the approximation to the perturbation operator α depicted in Figure 23. We can see that the locations of all interfaces and the size of the perturbation from one layer to another have been corrected and that the perturbation operator α is again very well approximated. Notice, in Figure 23, there are residual vertical lines that run all the way to the horizontal axis of the coordinate system. This is believed to be caused by Maple functions, the software

we used to perform the calculation. However, these residual lines do not alter the accuracy of the output approximation.

5.2 Model 2: Non-monotonic Velocity

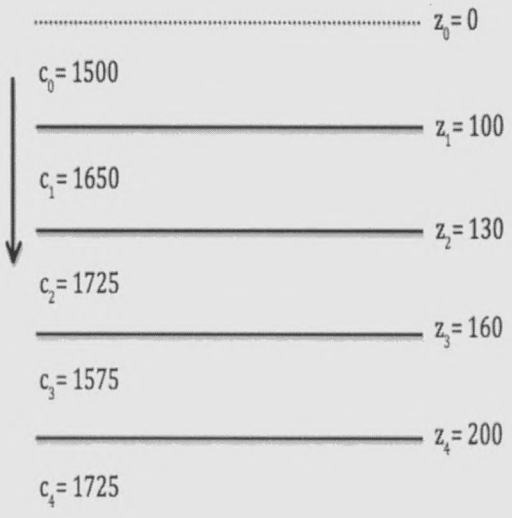

Figure 24: Earth Model 2

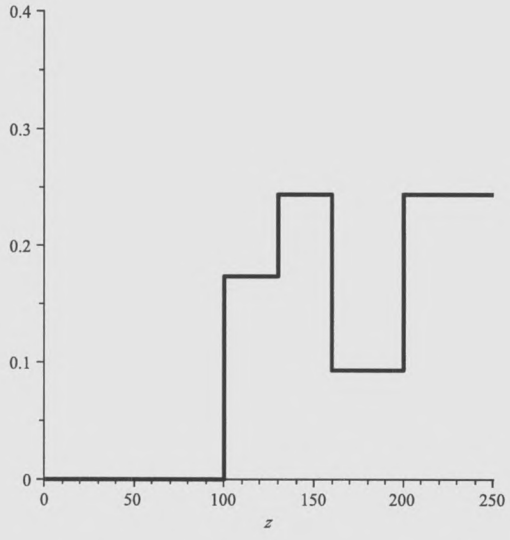

Figure 25: Perturbation Operator for Model 2

The second earth model, described in Section 4.4, is shown in Figure 24 and the perturbation operator α for this model is shown in Figure 25. The delta function data is (See Equation (47))

$$D = \frac{1}{21}\delta(t-100) + \frac{176}{3969}\delta\left(t - \frac{1400}{11}\right) - \frac{16192}{178605}\delta\left(t - \frac{38800}{253}\right) + \frac{8464}{93555}\delta\left(t - \frac{1017200}{5313}\right).$$

Entering this data into Equation (52) for α_1 yields the first approximation to the perturbation operator α, shown in Figure 26. Again, as expected, this initial step in the algorithm only finds the first interface accurately.

By plugging α_1 obtained in the first step into the algorithm in Equation (51), we obtained the approximation to the perturbation operator, depicted in Figure 27. We see that the locations of all interfaces and the size of the perturbations between each interface have now been corrected, showing that the perturbation operator α is very well approximated in

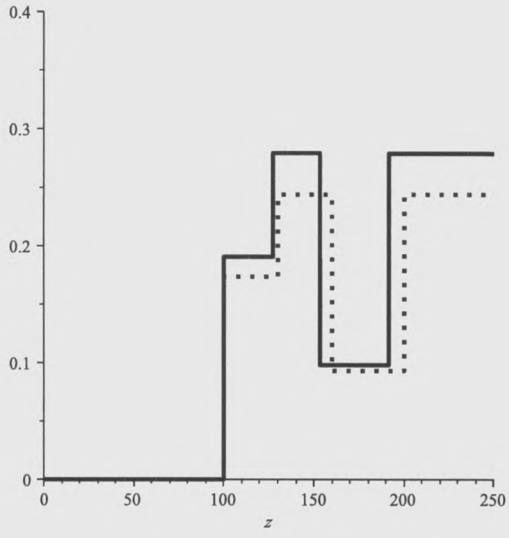

Figure 26: Plot of α_1 (solid) compared with α (dotted) for Model 2 and Dirac delta waveform input Data

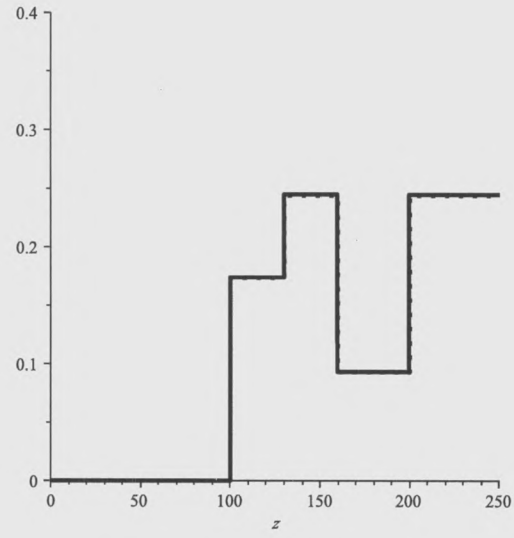

Figure 27: Plot of α^{SII} (solid) compared with α (dotted) for Model 2 and Dirac delta waveform input Data

this case too.

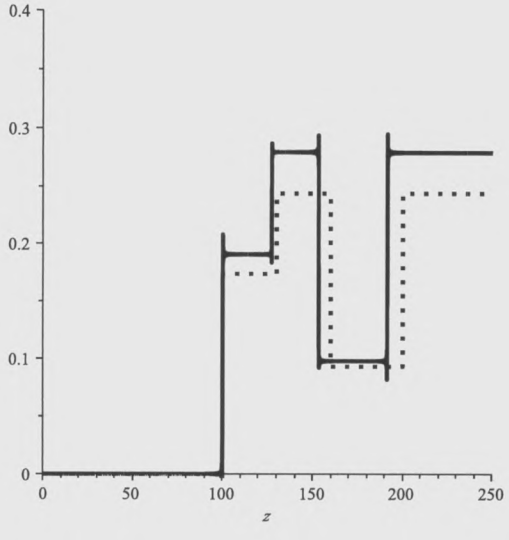

Figure 28: Plot of α_1 (solid) compared with α (dotted) for Model 2 and Sinc waveform input data

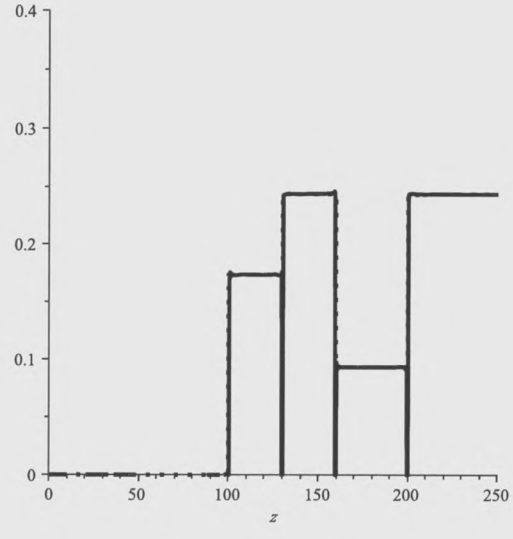

Figure 29: Plot of α^{SII} (solid) compared with α (dotted) for Model 2 and Sinc waveform input data

The band-limited wave propagation data for Model 2 is (See Equation(48))

$$\begin{aligned} D &= \frac{1}{21}Sinc(t-100)+\frac{176}{3969}Sinc\left(t-\frac{1400}{11}\right) \\ &- \frac{16192}{178605}Sinc\left(t-\frac{38800}{253}\right)+\frac{8464}{93555}Sinc\left(t-\frac{1017200}{5313}\right). \end{aligned}$$

We input this into Equation (52) and we got the first approximation to the perturbation operator, α, depicted in Figure 28. Once more, the first interface is located accurately but the location of the following interfaces and the size of the perturbation from one layer to the next is poorly determined.

Plugging the α_1 calculated into the algorithm in Equation (51), produces the approximation to the perturbation operator, shown in Figure 29. We see that the locations of all interfaces and the size of the perturbation between the interfaces have been calculated correctly, resulting in a very well approximation of the perturbation operator, α. Notice, again, in Figure 29, the residual vertical lines, similar to the lines shown in Figure 23. This is believed to be a consequence of the Maple functions we are using to perform the calculations. But, as mentioned before, these residual lines do not affect the accuracy of the approximation.

5.3 Model 3: Oscillating Velocity

The third earth model, described in Section 4.5 is shown in Figure 30 and the perturbation operator, α, is shown in Figure 31. The delta function data is (See Equation (49))

$$\begin{aligned} D &= \frac{7}{67}\delta(t-100)-\frac{39960}{623971}\delta\left(t-\frac{4600}{37}\right)+\frac{768830400}{12055743691}\delta\left(t-\frac{73120}{481}\right) \\ &- \frac{14792296896000}{232929023853811}\delta\left(t-\frac{88720}{481}\right)+\frac{284603792279040000}{4500421669879482331}\delta\left(t-\frac{106480}{481}\right) \\ &- \frac{5745776963448729600000}{86952647083741478117251}\delta\left(t-\frac{114280}{481}\right). \end{aligned}$$

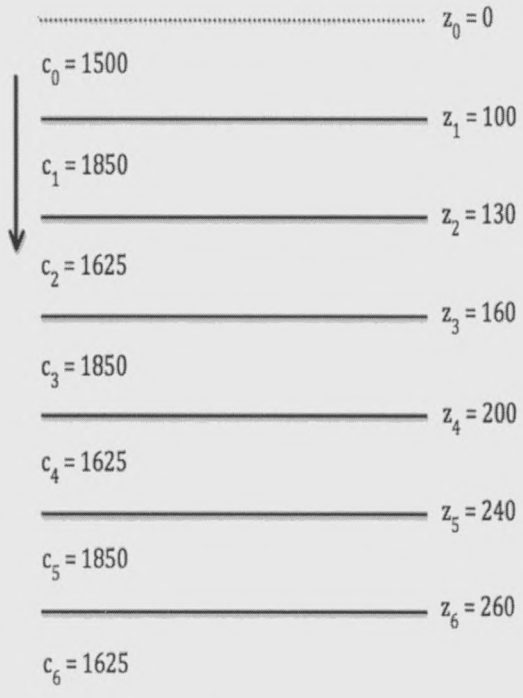

Figure 30: Earth Model 3

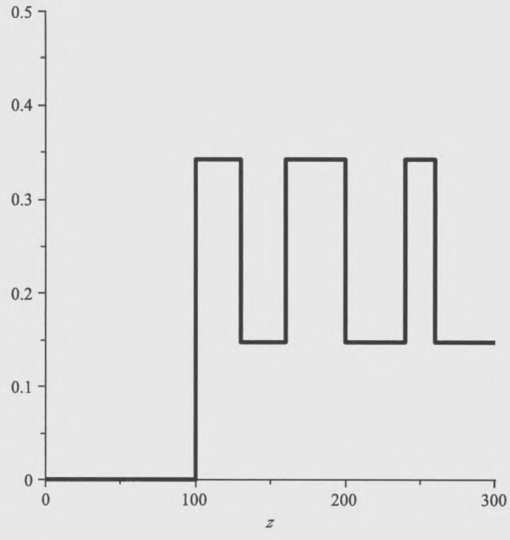

Figure 31: Perturbation Operator for Model 3

Plugging this data into Equation (52) for α_1 yields the first approximation to the perturbation operator α, shown in Figure 32. Again, this initial step in the algorithm only finds the first interface accurately. As mentioned in the previous sections, this is because the actual medium and the reference coincide up to the first interface but after that, the actual medium is different than the reference medium therefore causing the locations of the subsequent interfaces to be mislocated and size of the perturbation from one layer to the next to be miscalculated.

By plugging in α_1 obtained in the first step into the algorithm in Equation (51), we obtained the approximation to the perturbation operator, depicted in Figure 33. We see that the locations of all interfaces and the size of the perturbations between each interface have now been corrected, showing that the perturbation operator α is very well approximated.

The band-limited wave propagation data for Model 3 is (See Equation (50))

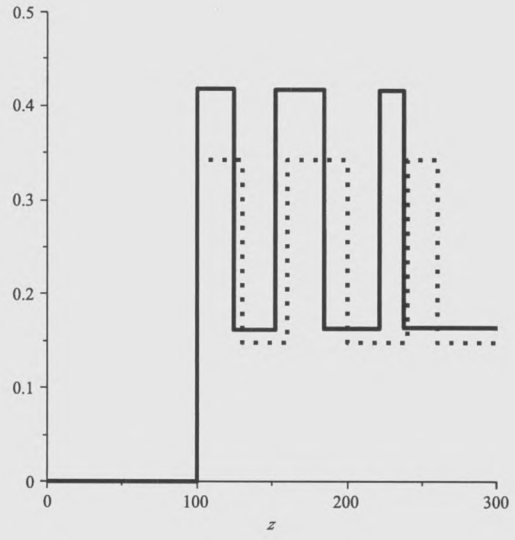

Figure 32: Plot of α_1 (solid) compared with α (dotted) for Model 3 and Dirac delta waveform input Data

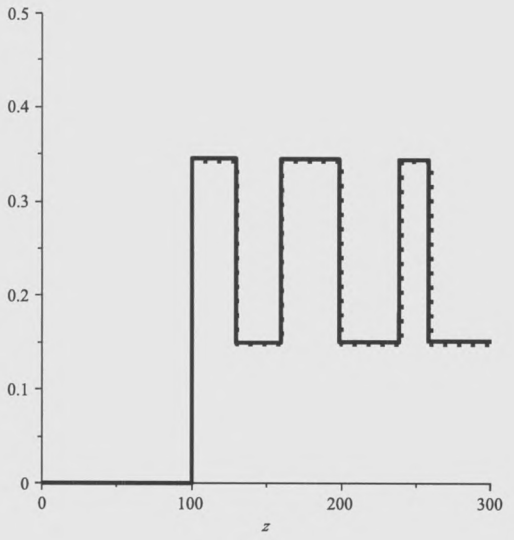

Figure 33: Plot of α^{SII} (solid) compared with α (dotted) for Model 3 and Dirac delta waveform input Data

$$
\begin{aligned}
D &= \frac{7}{67}Sinc\,(t-100) - \frac{39960}{623971}Sinc\left(t-\frac{4600}{37}\right) + \frac{768830400}{12055743691}Sinc\left(t-\frac{73120}{481}\right) \\
&- \frac{14792296896000}{232929023853811}Sinc\left(t-\frac{88720}{481}\right) + \frac{284603792279040000}{4500421669879482331}Sinc\left(t-\frac{106480}{481}\right) \\
&- \frac{5745776963448729600000}{86952647083741478117251}Sinc\left(t-\frac{114280}{481}\right).
\end{aligned}
$$

Plugging this into Equation (52) we obtain the first approximation to the perturbation operator, α, depicted in Figure 34. Once more, the first interface is located accurately but the location of the following interfaces and the size of the perturbation from one layer to the next is poorly determined.

Plugging the α_1 calculated in the first step into the algorithm in Equation (51), produces the approximation to the perturbation operator, shown in Figure 35. We see that the locations of all interfaces and the size of the perturbation between the interfaces have been corrected, resulting in a very good approximation of the perturbation operator, α.

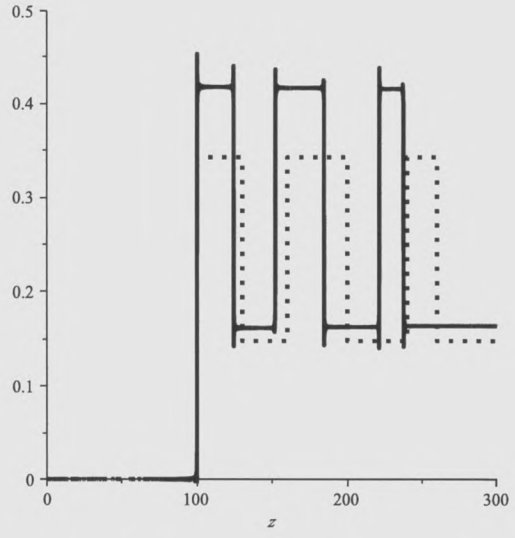

Figure 34: Plot of α_1 (solid) compared with α (dotted) for Model 3 and Sinc waveform input data

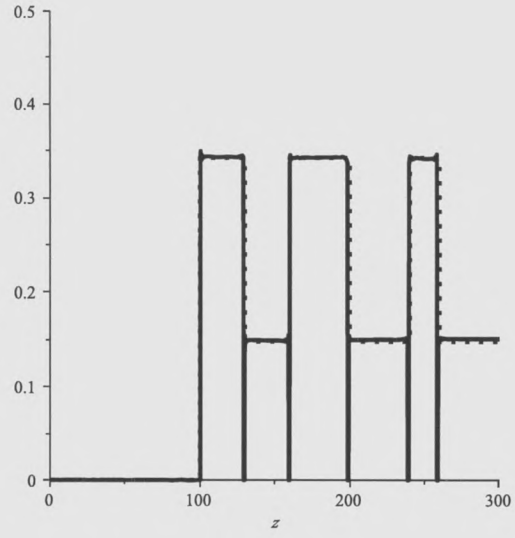

Figure 35: Plot of α^{SII} (solid) compared with α (dotted) for Model 3 and Sinc waveform input data

6 Comparison with the Leading Order Imaging Algorithm

In this chapter we compare the results we obtained in Chapter 5 with the results produced by the leading order imaging algorithm from [12]. We first apply this algorithm to the three models and two data types we discussed in the previous chapters. Then we use a fourth model to emphasize the differences between the two algorithms. Note that we are only comparing the imaging aspects of both algorithms since the leading order imaging algorithm only corrects the depths of the mislocated interfaces and does not change the amplitude of the perturbation operator.

The leading order imaging algorithm was shown in Chapter 3.2.1 to have the formula (See Equation (24))

$$\alpha^{IS_{LO}}(z) = \frac{1}{2\pi}\int_{-\infty}^{\infty} \alpha_1(k_0) e^{ik_0(z-\frac{1}{2}\int_0^z \alpha_1(z')dz')} dk_0, \tag{53}$$

where, as before,

$$\alpha_1(z) = 4\int_{-\infty}^{z} \mathbf{D}(z')dz' \tag{54}$$

and where $\mathbf{D}(z')$ represents the data that has been imaged to depth z'.

6.1 Model 1: Monotonic Increasing Velocity

First we are using the full frequency spectrum data generated by the Dirac delta function. As can be seen from the plot, the leading order imaging algorithm approximates the location of each interface very well. However, there is a slight error that can be noticed in the location of the second and third interface. This error increases as the contrast between the velocity of the actual layer and the reference velocity gets larger.

Next we use the band-limited data generated by the Sinc function. Notice that the results are very similar when using both the full spectrum and band-limited data. Both outputs show that the leading order imaging algorithm recovers the location of each interface nearly

Figure 36: Earth Model 1

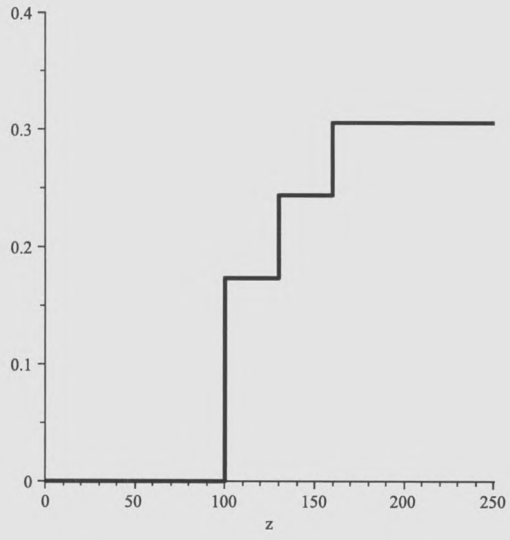

Figure 37: Perturbation Operator for Model 1

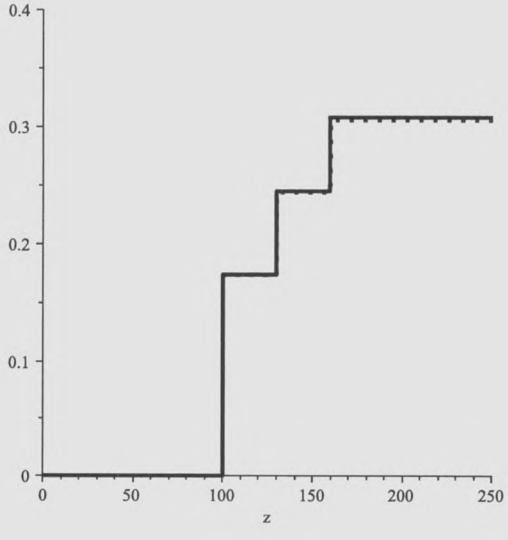

Figure 38: Plot of α^{SII} (solid) compared with α (dotted) for Model 1 and Dirac delta waveform input data

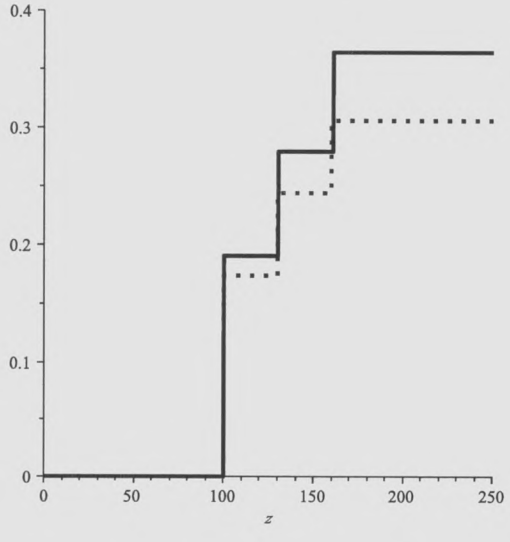

Figure 39: Plot of $\alpha^{IS_{LO}}$ (solid) compared with α (dotted) for Model 1 and Dirac delta waveform input data

perfect.

6.2 Model 2: Non-monotonic Velocity

For this second model we start again with the full frequency spectrum data generated by the Dirac delta function.

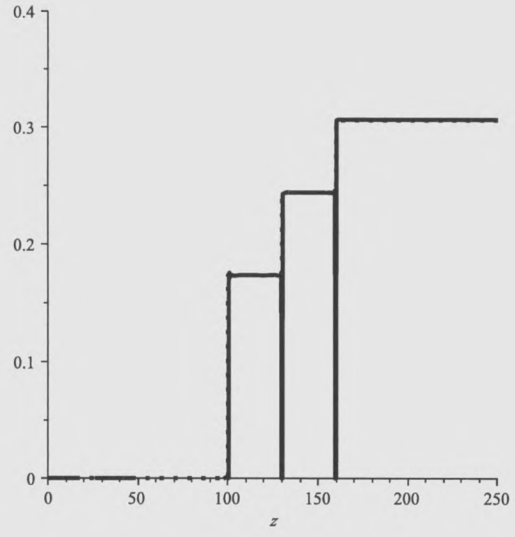

Figure 40: Plot of α^{SII} (solid) compared with α (dotted) for Model 1 and Sinc waveform input data

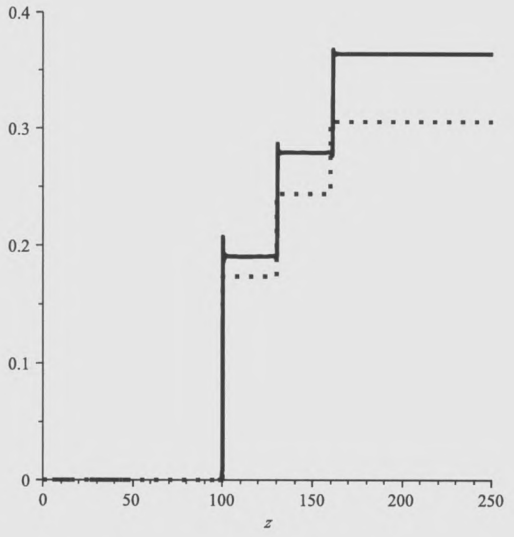

Figure 41: Plot of $\alpha^{IS_{LO}}$ (solid) compared with α (dotted) for Model 1 and Sinc waveform input data

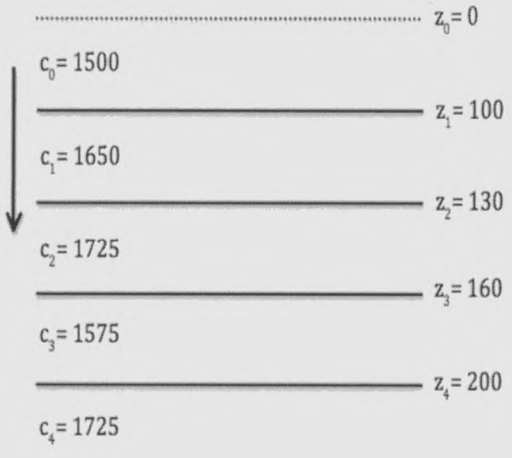

Figure 42: Earth Model 2

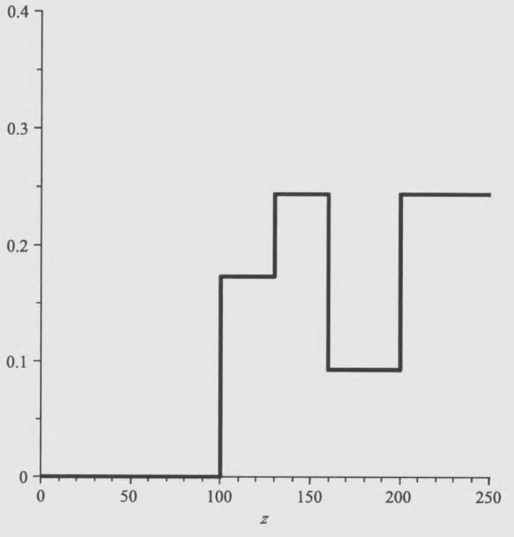

Figure 43: Perturbation Operator for Model 2

As can be seen from the plots, the leading order imaging algorithm approximates the location of each interface very well for this model too. The largest errors in this case can be seen at the second and fourth interface: this is because the contrast between the reference velocity and the velocity of the third and fifth layers respectively is the largest. Next we use the band-limited data generated by the Sinc function. In this case, the results and small

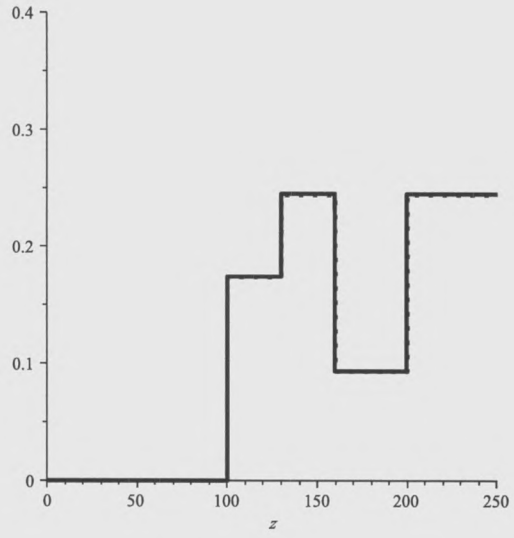

Figure 44: Plot of α^{SII} (solid) compared with α (dotted) for Model 2 and Dirac delta waveform input data

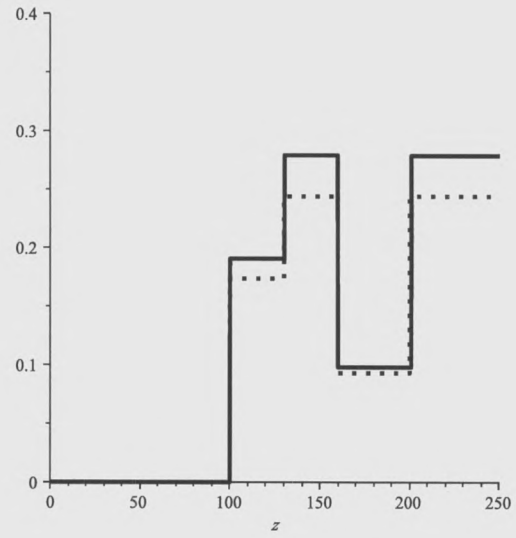

Figure 45: Plot of $\alpha^{IS_{LO}}$ (solid) compared with α (dotted) for Model 2 and Dirac delta waveform input data

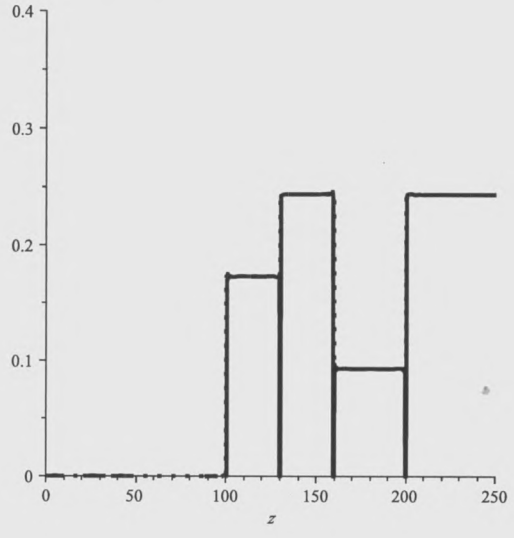

Figure 46: Plot of α^{SII} (solid) compared with α (dotted) for Model 2 and Sinc waveform input data

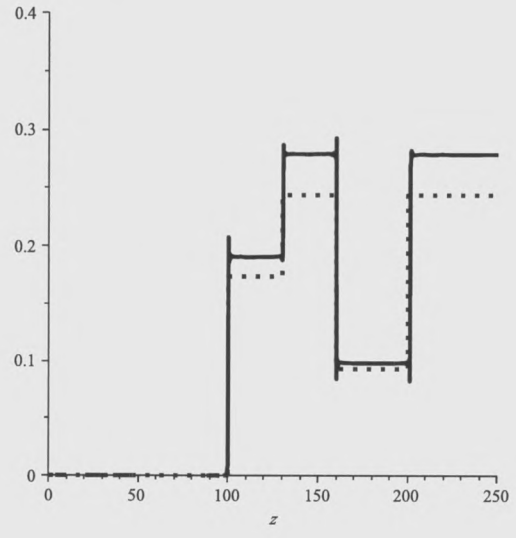

Figure 47: Plot of $\alpha^{IS_{LO}}$ (solid) compared with α (dotted) for Model 2 and Sinc waveform input data

errors are consistent with our previous observations.

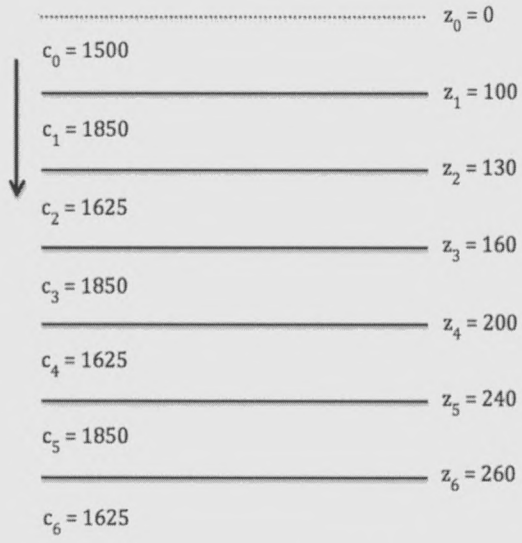

Figure 48: Earth Model 3

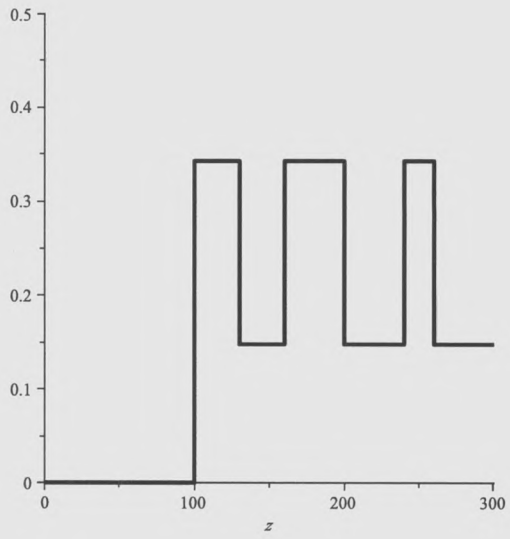

Figure 49: Perturbation Operator for Model 3

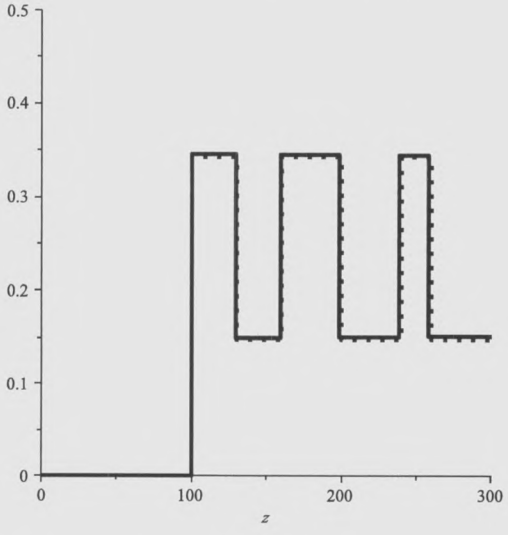

Figure 50: Plot of α^{SII} (solid) compared with α (dotted) for Model 3 and Dirac delta waveform input data

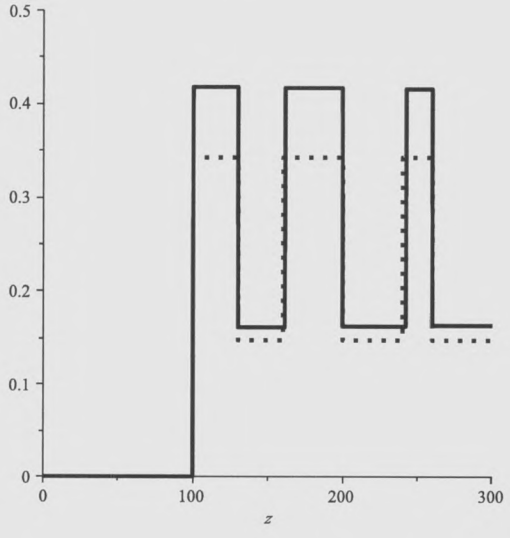

Figure 51: Plot of $\alpha^{IS_{LO}}$ (solid) compared with α (dotted) for Model 3 and Dirac delta waveform input data

6.3 Model 3: Oscillating Velocity

Again, we noticed that the leading order imaging algorithm approximated the locations of each interface for both full spectrum and band-limited data with a very small margin of error. As expected, the largest errors occur in the locations of the third and fifth interfaces, since the largest contrast between the reference velocity and the actual velocity occurs in

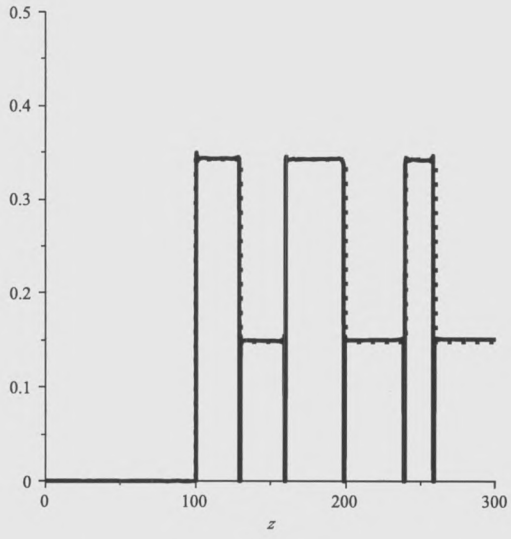

Figure 52: Plot of α^{SII} (solid) compared with α (dotted) for Model 3 and Sinc waveform input data

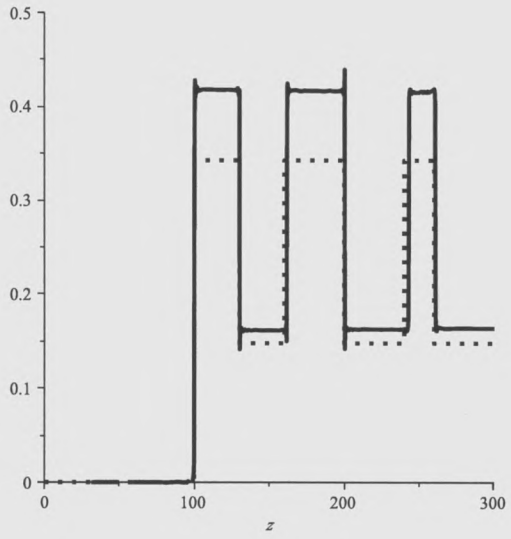

Figure 53: Plot of $\alpha^{IS_{LO}}$ (solid) compared with α (dotted) for Model 3 and Sinc waveform input data

the fourth and sixth layer respectively.

6.4 Model 4: Large Velocity Inversion

The fourth model that we are going to use for comparison was designed to exhibit a large contrast between the reference velocity and the velocity inside of one of the layers. We observed possible increased errors in the leading order imaging algorithm in the case of larger contrasts in previous sections. This test will allow us to understand better the similarities and differences between the two algorithms we are comparing.

The model consists of four interfaces located in water at depths of $z_1 = 100$, $z_2 = 150$, $z_3 = 175$ and $z_3 = 235$ with the sound velocity inside of the layers having the values $c_0 = 1500$, $c_1 = 1650$, $c_2 = 1725$, $c_3 = 1625$ and $c_4 = 2500$ (See Figure 54). The perturbation operator α for this earth model is shown in Figure 55.

The data in this case consists of four primary reflections and for a Dirac delta waveform

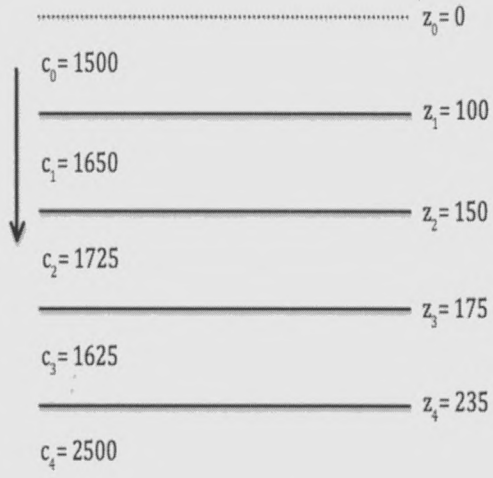

Figure 54: Earth Model 4

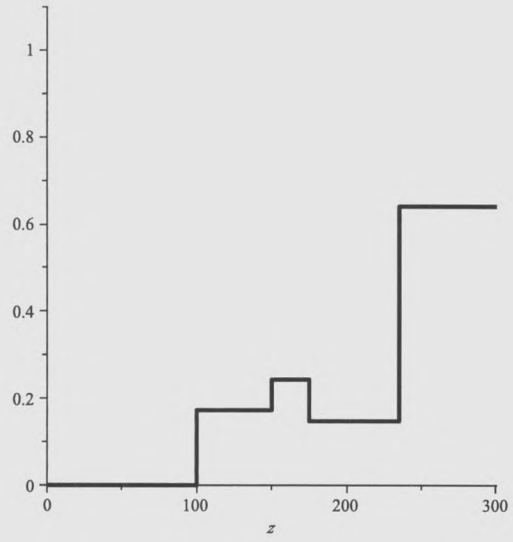

Figure 55: Perturbation Operator for Model 4

the it has the formula

$$\begin{aligned} D &= \frac{1}{21}\delta(t-100)+\frac{88}{3969}\delta\left(t-\frac{1600}{11}\right)-\frac{356224}{11966525}\delta\left(t-\frac{42300}{253}\right) \\ &+ \frac{772204576}{2512174581}\delta\left(t-\frac{732060}{3289}\right). \end{aligned} \tag{55}$$

The results from running the data through both algorithms are shown in Figures 56 and 57. We notice that the simultaneous imaging and inversion algorithm puts all interfaces at their correct locations, while the leading order imaging algorithm does not find the last interface correctly. Is clear that large contrasts between the reference velocity and the velocity inside of the actual medium affect the performance of the leading order imaging algorithm negatively. This effect is not felt by the simultaneous imaging and inversion algorithm.

$$\begin{aligned} D &= \frac{1}{21}Sinc(t-100)+\frac{88}{3969}Sinc\left(t-\frac{1600}{11}\right)-\frac{356224}{11966535}Sinc\left(t-\frac{42300}{253}\right) \\ &+ \frac{4841408}{22907367}Sinc\left(t-\frac{732060}{3289}\right) \end{aligned} \tag{56}$$

We ran the algorithms again this time using the Sinc function to see if the same results

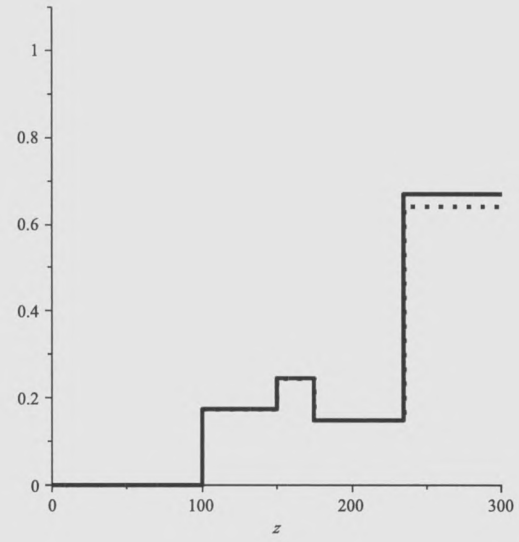

Figure 56: Plot of α^{SII} (solid) compared with α (dotted) for Model 4 and Dirac delta waveform input data

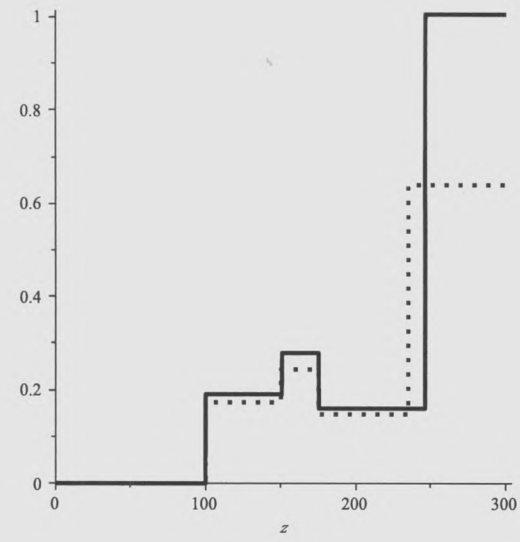

Figure 57: Plot of $\alpha^{IS_{LO}}$ (solid) compared with α (dotted) for Model 4 and Dirac delta waveform input data

occur when using band-limited data. In this case the data has the form

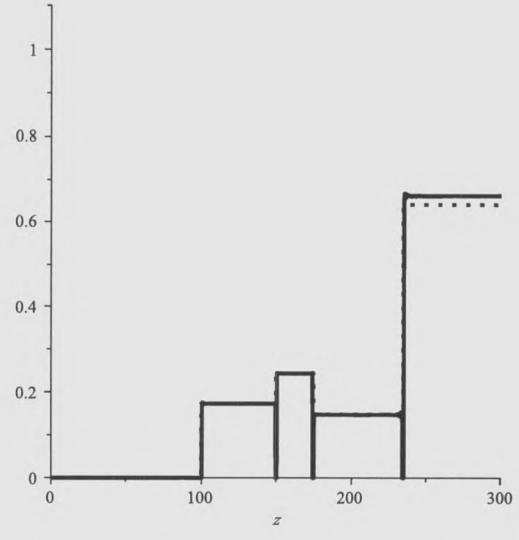

Figure 58: Plot of α^{SII} (solid) compared with α (dotted) for Model 4 and Sinc waveform input data

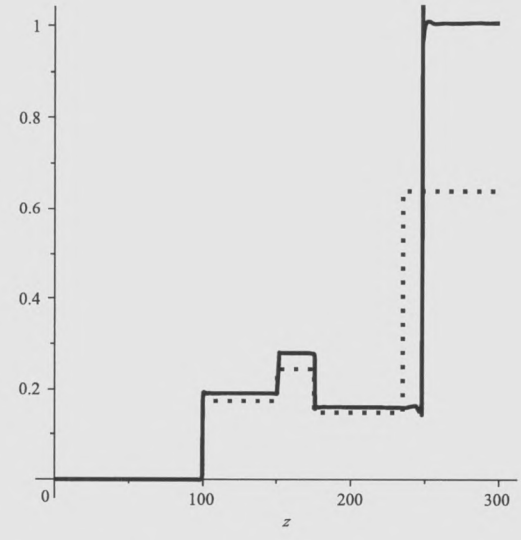

Figure 59: Plot of $\alpha^{IS_{LO}}$ (solid) compared with α (dotted) for Model 4 and Sinc waveform input data

The results from running the data through both algorithms are shown in Figures 58 and 59. As expected, we notice the same behavior of the algorithms with band-limited data as with full spectrum data. The leading order imaging algorithm does not locate the final

interface correctly while the simultaneous imaging and inversion algorithm was able to find all interfaces correctly.

7 Conclusions

In this thesis, we tested the capability and efficiency of an inverse scattering algorithm for imaging seismic data. The algorithm we investigated simultaneously images and inverts one-dimensional, one-parameter (velocity), acoustic reflection data. The algorithm does not require a velocity model or any other *a priori* information about the medium under investigation, the only input being a reference velocity (the speed of sound in water) and the data collected in the experiment.

In our tests, we used four earth model and two types of data, full spectrum impulse data and band-limited data. These choices exemplify different conditions that can be found in a one-dimensional medium with variable velocity. The results show that the algorithm can precisely locate the interfaces and discover the correct velocity changes at those interfaces for all models and data types. Finally, we compared the results from the simultaneous imaging and inversion (SII) algorithm with those from another inverse scattering algorithm presented in the literature, the leading order imaging algorithm. We discovered that the SII algorithm produces better results when the contrast between the reference velocity and the actual velocity inside of earth layers is large. This is explained by the fact that, besides the leading order imaging terms, the SII algorithm contains higher order imaging terms from the full inverse scattering series.

These results are promising and warrant further research. Some of the planned future research includes testing the stability of the SII algorithm using discrete data sets with or without random noise as well as the extension of the algorithm to include 1.5 and 2 dimensional earth models.

References

[1] L.C. ANDREWS (2003), *Mathematical Techniques for Engineers and Scientists*, SPIE Press, Washington.

[2] P.M. CARVALHO (1992), *Free Surface Multiple Reflection Elimination Method Based on Nonlinear Inversion of Seismic Data*, PhD Thesis, Department of Geosciences, Universidad Federal de Bahia, Houston, Salvador-Bahia, Brazil.

[3] R. EASTON (2010), *Fourier Methods in Imaging*, John Wiley and Sons, New York.

[4] F. LIU, B.G. NITA, A.B. WEGLEIN, K.A. INNANEN (2004), *Inverse scattering series for laterally-varying media*, Mission-Oriented Seismic Research Program, pp. 132-144.

[5] F. LIU, A.B. WEGLEIN, K.A. INNANEN, B.G. NITA (2005), *Extension of the nonlinear depth imaging capability of the inverse scattering series to multidimensional media: strategies and numerical results*, Sociedade Brasileira de Geofsica (SBGf) Expanded Abstracts.

[6] F. LIU, A.B. WEGLEIN, K. INNANEN AND B.G. NITA (2006), *Multi-dimensional seismic imaging using the inverse scattering series. SEG Expanded Abstracts*, 76th Annual Meeting of the Society of Exploration Geophysicists, New Orleans, Louisiana.

[7] F. LIU, A.B. WEGLEIN, K.A. INNANEN, B.G. NITA, J. ZHANG (2007), *A comprehensive strategy for removing multiples and depth imaging primaries without subsurface information: Direct horizontal common image gathers without the velocity or "ironing"*, SEG, Expanded Abstracts, pp. 2210-2214.

[8] J.D. LOGAN, *Applied Partial Differential Equations*, Springer, New York.

[9] B.G. NITA (2004), *Inverse scattering series for a 2D acoustic medium*, preliminary report.

[10] B.G. NITA (2009), *An algorithm for seismic imaging and amplitude correction derived from scattering theory*, International Journal of Tomography and Statistics, 12, FO9, pp. 3-18.

[11] S.A. SHAW, A.B. WEGLEIN, D.J. FOSTER, K.H. MATSON, AND R.G. KEYS (2003), *Isolation of a leading order depth imaging series and analysis of its convergence properties*, Mission Oriented Seismic Research Program, Annual Report 2.

[12] S.A. SHAW (2005), *An inverse scattering series algorithm for depth imaging of reflection data*, PhD Thesis, Department of Geosciences, University of Houston, Houston, TX.

[13] J.R. TAYLOR (1972), *Scattering theory*, John Wiley and Sons, New York.

[14] A.B. WEGLEIN, F.A. GASPAROTTO, P.M. CARVALHO, R.H. STOLT (1997), *An inverse scattering series for attenuating multiples in seismic reflection data,* Geophysics, 62, pp. 1975-1989.

[15] A.B. WEGLEIN, K.H. MATSON, D.J. FOSTER, S.A. SHAW, P.M. CARVALHO, D. CORRIGAN (2002), *Predicting the correct spatial location of reflectors without knowing or determining the precise medium and wave velocity: initial concept, algorithm and analytic and numerical example,* Journal of Seismic Exploration, 10, pp. 367-382.

[16] A.B. WEGLEIN, F. A. ARAUJO, P. M. CARVALHO, R. H. STOLT, K. H. MATSON, R. COATES, D. CORRIGAN, D. J. FOSTER, S. A. SHAW, H. ZHANG (2003), *Inverse scattering series and seismic exploration,* Topical Review Inverse Problems, 19, pp. R27-R83.

[17] H. ZHANG (2006),*Direct non-linear acoustic and elastic inversion : towards fundamentally new comprehensive and realistic target identification*, PhD Thesis, Department of Physics, University of Houston, Houston, TX.